

Remarkably boosting ethanol upgrading to higher alcohols through cooperative catalysis of surface-interface multiple-active sites on nitrogen-doped carbon decorated copper-based catalysts

Liyuan Yuan, Ming Zhang, Guoli Fan, Feng Li ^{*}

State Key Laboratory of Chemical Resource Engineering, Beijing University of Chemical Technology, Beijing 100029, China



ARTICLE INFO

Keywords:

Ethanol
Guerbet reaction
Interfacial Cu⁺ sites
Surface modification of nitrogen-doped carbon
Higher alcohols

ABSTRACT

Upgrading biomass-derived ethanol to higher alcohols is a significantly promising process involving multi-step tandem reactions finely regulated by multiple active sites. However, the role of multiple active sites in addressing activity and selectivity toward alcohols still remains unclear. Herein, we developed supported copper catalysts decorated with surface trace-level nitrogen-doped carbon (NC) derived from melamine/Cu-Mg-Al layered double hydroxide composite precursors and studied their catalytic performance for converting ethanol to higher alcohols. As-constructed NC-decorated Cu-based catalyst, which was obtained by calcination of the precursor with a melamine/Cu molar ratio of 2:1 at 550 °C, achieved an 82% selectivity to higher alcohols at 63% ethanol conversion under reaction conditions (250 °C, 2 MPa pressure), along with unprecedentedly high ethanol conversion rate of 38.9 mmol·g⁻¹·h⁻¹ and production rate of higher alcohols (31.9 mmol·g⁻¹·h⁻¹), which are the highest standard among previously reported catalysts to date. By performing comprehensive structural characterizations and density functional theory calculations, it was revealed that surface modification of NC component promoted the dispersion of Cu particles and modulated the electronic structures of Cu species, facilitating the formation of Cu⁺ sites at metal-support interfaces and surface oxygen vacancies. Moreover, the significantly enhanced catalytic efficiency of Cu catalysts was mainly attributed to the favorable cooperative catalysis of multiple surface-interface active sites (Cu⁰, Cu⁺, oxygen vacancies, and acid-base sites), thereby accelerating tandem processes to produce higher alcohols during ethanol conversion. The present findings afford a new strategy for the rational design of high-performance supported copper catalysts for biomass-derived ethanol coupling to higher alcohols.

1. Introduction

To directly address the challenges associated with the increasing consumption of non-renewable fossil resources, serious environmental pollution, and climate change caused by massive carbon dioxide emissions, it is important to accelerate the development and utilization of renewable resources. Biomass-derived ethanol is a promising fuel that can be produced sustainably through various processes such as fermentation of carbohydrates, petroleum refining or syngas conversion [1–3]. Due to increased energy demand and the commercialization of large-scale sustainable ethanol production, a widespread topic of interest has been paid to the selective conversion of ethanol into higher-value-added long-chain chemicals as an alternative to traditional fossil feedstocks [4–6]. Currently, heterogeneous catalysts have

advanced the transformation of ethanol into a range of components such as acetaldehyde [7–9], ethyl acetate [10], olefins [11–13], and alcohols [14–16]. In particular, upgrading ethanol to higher alcohols has become a topic of great interest, because higher alcohols with higher energy density and lower water absorption are a highly promising fuel with unmatched advantages and can be used as feedstock for the production of important chemicals and long-chain hydrocarbons [17].

Commonly, upgrading ethanol to higher alcohols involves series of tandem reactions (Guerbet reaction), which consist of dehydrogenation, aldol condensation, dehydration, and hydrogenation [18–20]. In such multi-step catalytic processes, multiple-active sites on heterogeneous catalysts work together and cooperate to catalyze the synthesis of long-chain oxygenates. For instance, amphoteric catalysts with adjustable acid-base properties, such as Mg-Al mixed metal oxides derived

* Corresponding author.

E-mail address: lifeng@mail.buct.edu.cn (F. Li).

from hydrotalcite [21–23], hydroxyapatite [24,25], and metal oxides modified Al_2O_3 [26], have been systematically investigated for upgrading ethanol to higher alcohols, wherein basic sites, particularly moderate or strong Lewis basic sites, are typically responsible for the aldol condensation process, and acidic sites are necessary for the dehydration process. Additionally, incorporating transition metals (e.g., Cu [27–30], Ni [31], and Co [32]) into catalysts can effectively reduce the reaction temperature required for ethanol activation and significantly enhance ethanol dehydrogenation and hydrogenation activity, due to cooperative catalysis between metallic sites and acid-base sites [33,34]. Due to their potent C-C cleavage abilities, however, the introduction of nickel and cobalt can also trigger undesirable side reactions, resulting in the generation of excessive gaseous by-products. For Cu-based catalysts, their weaker ability to crack C-C bonds can effectively prevent severe decarbonylation or methanation during ethanol conversion. It is worth noting that copper plays a pivotal role in promoting alcohol dehydrogenation and determining selectivity to alcohols or esters due to the coexistence of Cu^0 and Cu^+ species [20]. In this regard, to promote ethanol upgrading to higher alcohols, most of the current studies focus on tailoring metal active sites or surface acid-base properties of copper-based catalysts [14,27,29,34]. However, it is difficult to regulate only one type of active site to achieve both high ethanol conversion and selectivity of higher alcohols. Therefore, designing high-performance copper-based catalysts with a favorable cooperative catalysis of multiple-active sites for highly efficient upgrading of ethanol to higher alcohols remains a huge challenge.

Considering that nitrogen-doped carbon (NC) component can be applied as excellent basic supports to efficiently regulate metal-support interactions and enhance metal dispersion [35–37], in this study, series of NC-decorated supported copper catalysts were fabricated via a melamine/Cu-Mg-Al layered double hydroxide (LDH) composite precursor method for ethanol coupling to higher alcohols including n-butanol. It was found that surface-interface structures of Cu-based catalysts could be easily tailored by incorporating trace-level NC component and controlling calcination temperature for precursors, thereby effectively modulating adsorption behaviors of ethanol and acetaldehyde intermediate and thus regulating the catalytic activity of the catalysts. As-constructed NC-decorated copper catalyst, which was obtained by calcination of the precursor with a melamine/Cu molar ratio of 2:1 at 550 °C, achieved an unprecedentedly high production rate of higher alcohols ($31.9 \text{ mmol}\cdot\text{g}_{\text{cat}}^{-1}\cdot\text{h}^{-1}$), outperforming all previously reported metal-based catalysts. The current strategy for the development of high-performance Cu-based catalysts offers a practical and direct solution for boosting ethanol upgrading to higher alcohols.

2. Experimental section

2.1. Preparation of catalysts

Melamine/CuMgAl-LDH composite precursors were prepared by the coprecipitation method with a microliquid film (MLF) reactor [38]. First, a 150 mL of metal salt solution (solution A) containing $\text{Cu}(\text{NO}_3)_2\cdot 6 \text{ H}_2\text{O}$, $\text{Mg}(\text{NO}_3)_2\cdot 6 \text{ H}_2\text{O}$, and $\text{Al}(\text{NO}_3)_3\cdot 9 \text{ H}_2\text{O}$ with a set molar ratio of 0.5:3:1 was prepared. Meanwhile, a base solution (150 mL, solution B) containing Na_2CO_3 (0.2 M) and NaOH (0.75 M) was prepared. Both solutions were poured simultaneously into the MLF reactor and stirred vigorously for 5 min at a rotor speed of 3500 rpm. Next, a certain amount of melamine at a set melamine/Cu molar ratio of x ($x = 0, 1, 2, 3$) was added into the synthesis suspension before stirring vigorously at 60 °C for 12 h. The resulting suspension was centrifuged, washed until the pH reached 7.0 ± 0.2 , and further dried in air at 60 °C overnight to obtain melamine/LDH precursors. The precursors were subsequently treated at various temperatures for 6 h in a nitrogen atmosphere and then reduced at 300 °C for 2 h in a flow of 10% H_2/N_2 . The resulting samples were named Cu-NC- x -T, where T represents the calcination temperatures (T = 450, 550, 650, and 750 °C). In addition, the precursor

with a melamine/Cu molar ratio of 2.0 was calcinated at 550 °C in air and subsequently reduced in 10% H_2/N_2 atmosphere at 300 °C for 2 h to obtain Cu-NC-2-550(A) comparison catalyst.

2.2. Sample characterization

Various characterizations including powder X-ray diffraction (XRD), low-temperature N_2 adsorption-desorption, transmission electron microscopy (TEM), scanning transmission electron microscopy (STEM), X-ray photoelectron spectroscopy (XPS), X-ray absorption fine-structure spectroscopy (XAFS), hydrogen temperature programmed reduction ($\text{H}_2\text{-TPR}$), temperature programmed desorption with CO_2 , NH_3 , or H_2 as probe molecules ($\text{CO}_2\text{-TPD}$, $\text{NH}_3\text{-TPD}$, or $\text{H}_2\text{-TPD}$), temperature programmed decomposition (TPDE), N_2O titration, in situ Fourier transform infrared spectroscopy (FT-IR) for pyridine adsorption, and in situ diffuse reflectance infrared Fourier transform (DRIFT) spectroscopy for CO adsorption, ethanol, and acetaldehyde, were carried out. The detailed information is provided in [Supporting information](#).

2.3. Calculation method

The density functional theory calculations with projector augmented wave were performed via VASP in this study [39,40]. The exchange-correlation effects were applied by the Perdew-Burke-Ernzerhof functional [41], while DFT+D3 was used for handling weak interactions [42]. The cut-off energy for the plane-wave basis was 450 eV. K-points were $2 * 2 * 1$ in the Brillouin zone. Energy and maximum stress were converged to 10–5 eV and 0.02 eV/Å, respectively.

2.4. Catalytic evaluations

Catalytic conversion of ethanol was performed in the tubular fixed-bed reactor (length 800 mm, inner diameter 10 mm) with a back-pressure regulator ([Fig. S1](#)). In a typical experiment, 1.0 g of calcined catalyst was squeezed and sieved into granules with 20–40 mesh, filled with a certain amount of quartz sand in the reactor, and then reduced at 300 °C for 2 h in a mixed flow of H_2/N_2 (v: v=1:9). Subsequently, nitrogen was injected into the reactor to remove excess hydrogen until cooled to the target temperature. Prior to entering the reactor, ethanol was fed into an evaporation oven preheated at 200 °C by a high-pressure liquid pump at 40 $\mu\text{L}/\text{min}$, with N_2 co-feed at 40 mL/min. The reaction was maintained under the desired conditions until a steady state was reached (10 h). Then the products were kept heated at > 200 °C before flowing to vent or to the preheated autosampler through a three-way valve, then monitored on-line by a gas chromatograph (GC) equipped with a flame ionization detector (FID, with a FFAP column (30 m × 0.32 mm)) and a thermal conductivity detector (TCD, with a HP-PLOT/Q column (30 m × 0.32 mm)). The products were simultaneously detected by TCD and FID detectors every 0.5 h via a six-way valve in the autosampler. The obtained products were further identified by GC-MS, and the relative correction factors of each product were quantitatively calculated by internal standard method. Ethanol conversion (Conv), product selectivity (Select), rate of ethanol conversion (r), and space-time yield of higher alcohols (STY) were calculated by [Eq. \(1–4\)](#) as follows:

$$\text{Conv}(\%) = \left(1 - \frac{\text{Remaining molar amount of ethanol}}{\text{Total molar amount of ethanol}} \right) \times 100 \quad (1)$$

$$\text{Select}(\%) = \frac{\text{Molar amount of carbon in the target product}}{\text{Molar amount of carbon in converted ethanol}} \times 100 \quad (2)$$

$$r(\text{mmol} \cdot \text{g}_{\text{cat}}^{-1} \cdot \text{h}^{-1}) = \frac{F_{\text{EtOH,in}}}{W_{\text{cat}}} \times \text{Conv} \quad (3)$$

$$\text{STY}(\text{mmol} \cdot \text{g}_{\text{cat}}^{-1} \cdot \text{h}^{-1}) = \frac{F_{\text{EtOH,in}}}{W_{\text{cat}}} \times \text{Conv} \times \text{Select}_{\text{HA}} \quad (4)$$

where $F_{\text{EtOH,in}}$ is the molar flow of ethanol in the inlet ($\text{mmol} \cdot \text{h}^{-1}$), $\text{Select}_{\text{HA}}$ is the selectivity of higher alcohols in the outlet, and W_{cat} (g) is the catalyst weight.

3. Results and discussion

3.1. Catalytic activity in the conversion of ethanol

As illustrated in Fig. 1A, the conversion of ethanol to higher alcohols (Guerbet reaction) typically involves tandem reactions consisting of ethanol dehydrogenation, acetaldehyde condensation, dehydration, and hydrogenation [43], accompanied by dehydrogenation coupling reaction to produce ethyl acetate (EA) as the main side reaction. Various NC-decorated Cu-based obtained at the calcination temperature of 550 °C were first evaluated in the continuous conversion of ethanol to higher alcohols at 250 °C and 4 MPa of reaction pressure. As depicted in

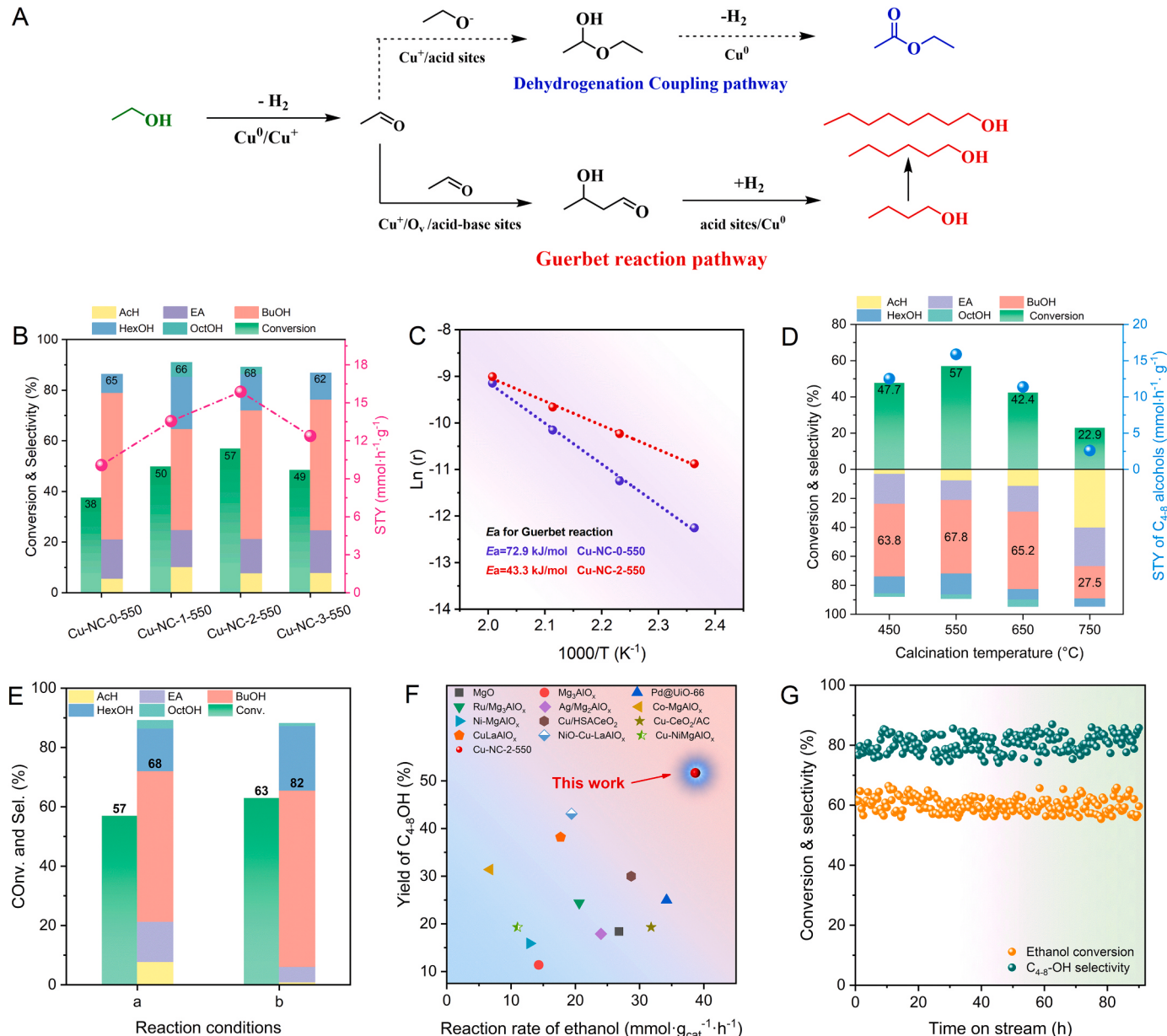


Fig. 1. (A) Schematic representation for reaction paths of ethanol conversion. (B) Comparison of catalytic performance in Guerbet reaction over different NC-decorated Cu-based catalysts (AcH = acetaldehyde, EA = ethyl acetate, BuOH = n-butanol, HexOH = n-hexanol, OctOH = n-octanol; other by-products include butyl acetate, ethyl butyrate, 1,1-diethoxyethane, 2-ethyl-butanol, 2-ethyl hexanal). (C) Arrhenius plots of reaction rate of Guerbet reaction over Cu-NC-0-550 and Cu-NC-2-550 catalysts. (D) Effect of calcination temperature for precursors on the catalytic performance of different Cu-NC-2-T catalysts. Reaction conditions: 250 °C; LHSV of 2.4 $\text{mL} \cdot \text{g}_{\text{cat}}^{-1} \cdot \text{h}^{-1}$; 4 MPa; and N_2 atmosphere; (E) Catalytic performance of Cu-NC-2-550 under different reaction conditions: (a) 250 °C, LHSV of 2.4 $\text{mL} \cdot \text{g}_{\text{cat}}^{-1} \cdot \text{h}^{-1}$, 4 MPa, and N_2 atmosphere; (b) 250 °C, LHSV of 3.6 $\text{mL} \cdot \text{g}_{\text{cat}}^{-1} \cdot \text{h}^{-1}$, 2.0 MPa, and N_2 atmosphere. (F) Comparison of yield of higher alcohols versus ethanol reaction rate reported in this work and in the literature in continuous Guerbet reaction in fixed bed reactor. (G) Stability test of Cu-NC-2-550 catalysts in upgrading ethanol to higher alcohols at 250 °C, 2.0 MPa, LHSV of 3.6 $\text{mL} \cdot \text{g}_{\text{cat}}^{-1} \cdot \text{h}^{-1}$, and N_2 atmosphere.

Fig. 1B, the unmodified Cu-NC-0–550 catalyst exhibits poorer catalytic activity with a low ethanol conversion of 38% compared to NC-decorated Cu-based catalysts. Notably, as the melamine/Cu molar ratio in precursors increases from 1:1–3:1, ethanol conversion first increases and then declines. Accordingly, Cu-NC-2–550 catalyst achieves a highest conversion of 57%. Of all Cu-based catalysts, however, no significant change in selectivity to higher alcohols ($C_{4-8}\text{-OH}$) is observed, maintaining selectivity to higher alcohols at 65–68%. Therefore, with the increasing melamine/Cu molar ratio in precursors, the space-time yield (STY) of higher alcohols also shows a similar change trend with ethanol conversion. As for Cu-NC-2–550 catalyst, the overall space-time yield for $C_{4-8}\text{-OH}$ reaches the maximum of $16 \text{ mmol}\cdot\text{g}_{\text{cat}}^{-1}\cdot\text{h}^{-1}$, further suggesting that the introduction of proper amount of melamine into catalyst precursors can significantly promote the Guerbet reaction of ethanol. However, more melamine introduced may be detrimental to the surface exposure of active sites, thereby inhibiting ethanol conversion and the formation of higher alcohols. Meanwhile, it is noted that despite a slight difference in total selectivity to $C_{4-8}\text{-OH}$, the introduction of melamine into precursors may effectively promote C-C coupling to produce long-chain alcohols with higher carbon numbers (**Fig. 1B** and **Table S1**) [44], but this trend becomes less evident with the increase of melamine/Cu molar ratio. However, compared to Cu-NC-2–550, Cu-NC-2–550(A) catalyst obtained by calcining the precursor at 550 °C in air achieves poorer catalytic performance (**Fig. S2**), along with a lower selectivity to higher alcohols (60%) at 39.0% ethanol conversion, further confirming the promotional effect of the introduction of melamine into catalyst precursors on ethanol conversion and the formation of higher alcohols. Further, the temperature dependence of the rate of ethanol conversion was investigated to determine the apparent activation energy (E_a) for total Guerbet reaction under reaction conditions (0.1 g catalyst, 150–225 °C, LHSV of $2.4 \text{ mL}\cdot\text{g}_{\text{cat}}^{-1}\cdot\text{h}^{-1}$, 4.0 MPa, N_2 atmosphere, and ethanol conversion <10%), a kinetic descriptor of structure–activity relationships independent of the type and number of reaction active sites (**Fig. 1 C**). Notably, compared to Cu-NC-0–550 (72.9 kJ/mol), Cu-NC-2–550 exhibits a lower apparent activation energy of 43.3 kJ/mol for the total Guerbet reaction, further indicating the presence of favorable active sites on the Cu-NC-2–550 for the Guerbet reaction of ethanol.

Furthermore, the influence of calcination temperature for the composite precursor with the 2:1 melamine/Cu molar ratio on the catalytic activity of supported copper catalysts was evaluated. As displayed in **Fig. 1D**, a volcano-type change trend is observed for both ethanol conversion and total selectivity of $C_{4-8}\text{-OH}$, where both the maximum values are achieved at a calcination temperature of 550 °C (57% and 68%, respectively). In contrast, the selectivity of acetaldehyde increases steadily with an increase in calcination temperature, ranging from 3.3% at 450 °C to 40.3% at 750 °C. This suggests a decline in the catalytic activity in coupling acetaldehyde to higher alcohols, which is possibly due to the collapse of the porous structure at higher pyrolysis temperatures and a subsequent reduction in active sites [45]. Conversely, the selectivity of ethyl acetate exhibits an opposite trend to that of higher alcohols with an increase in calcination temperature. These results demonstrate that adjusting calcination temperature can further regulate product distribution, which is strongly influenced by surface-interface structures of catalysts modulated by varying calcination temperature.

Fig. S3 further illustrates the catalytic activity of Cu-NC-2–550 catalyst as a function of the reaction temperature, showing an obvious enhancement in conversion from 14.5% at 200 °C to 79.4% at 300 °C due to the beneficial promotional effect of elevated temperature on ethanol conversion. However, selectivity towards higher alcohols displays a volcano-type behavior as a consequence of undesired side reactions at high temperatures. Considering that ethanol dehydrogenation usually is identified as the rate-determining step of the whole Guerbet reaction, reaction conditions were further optimized by reducing reaction pressure, increasing reactant concentration, and increasing contact time to accelerate the dehydrogenation and subsequent condensation

rate. Typically, the decrease in reaction pressure is conducive to the occurrence of ethanol dehydrogenation process during the Guerbet reaction of ethanol, while a higher space velocity of ethanol liquid is beneficial for its use as a hydrogen donor to promote the hydrogenation of reaction intermediates to form higher alcohols. As shown in **Fig. 1E**, the conversion efficiency of ethanol for Cu-NC-2–550 catalyst is further enhanced by reducing the reaction pressure and increasing the space velocity of ethanol liquid, which promotes the dehydrogenation of alcohols and subsequently the condensation reaction. Consequently, the catalyst achieves an 82% selectivity to higher alcohols at a high ethanol conversion of 63% under reaction conditions (250 °C, LHSV of $3.6 \text{ mL}\cdot\text{g}_{\text{cat}}^{-1}\cdot\text{h}^{-1}$, 2 MPa reaction pressure), along with exceptionally high ethanol conversion rate of $38.9 \text{ mmol}\cdot\text{g}_{\text{cat}}^{-1}\cdot\text{h}^{-1}$ and STY of higher alcohols ($31.9 \text{ mmol}\cdot\text{g}_{\text{cat}}^{-1}\cdot\text{h}^{-1}$), surpassing those obtained over all supported metal catalysts previously reported (**Fig. 1F** and **Table 1**).

In addition, the stability of Cu-NC-2–550 catalyst was evaluated in the upgrading of ethanol at 250 °C and 2 MPa (**Fig. 1G**). Notably, the Cu-NC-2–550 catalyst exhibits appreciable activity without any deactivation up to 90 h. These results demonstrate the exceptional stability of the Cu-NC-2–550 catalyst, which can be attributed to the inhibition of surface NC component on copper particle aggregation and growth originating from strong interactions between Cu species and the support containing NC component in the catalyst.

3.2. Structural analysis

In present study, surface NC-decorated Cu-based catalysts (Cu-NC-x) were fabricated by thermal decomposition of the composite precursor of ternary CuMgAl-LDH and melamine with different melamine/Cu molar ratios at different temperatures (**Fig. 2A**). First, XRD patterns for melamine/CuMgAl-LDH precursors with different melamine/copper molar ratios exhibit several characteristic diffraction peaks ascribed to hydrotalcite-like materials (JCPDS 89–0460) and melamine (**Fig. S4**). After calcination at 550 °C and subsequent reduction treatment, characteristic diffraction peaks for metallic copper (JCPDS no.04–0836) and MgO (JCPDS no.045–0946) phases are observed (**Fig. S4**). As the calcination temperature increases for samples with the melamine/copper molar ratio of 2:1 in precursors, metallic copper and MgO phases present a gradually enhanced trend in diffraction intensity (**Fig. 2B**), indicative of the increased size of Cu^0 or MgO particles due to the improved growth of particles at higher temperatures [53]. In addition, a broad peak assignable to CuO phase (JCPDS no.05–0661) is observed around 35°. Specifically, spinel-type MgAl_2O_4 (JCPDS no.082–2424) may also be formed in Cu-NC-2–750. However, in all cases, no peaks assigned to crystalline Al_2O_3 or C_3N_4 phases are detected, possibly owing to the formation of high dispersive amorphous alumina [54] or a trace amount of C-containing component (**Table 2**). In these cases, high dispersive amorphous alumina in samples can act as a dispersant to suppress Cu particle aggregation to a large extent. Further increasing the calcination temperature results in the increased size of Cu crystallites, which is calculated based on XRD broadening of the Cu (111) deconvolution results, gradually increasing from 5.6 nm at 550 °C to 26.5 nm at 750 °C. Furthermore, based on N_2 adsorption-desorption isotherms of Cu-based samples (**Fig. S5**), it is revealed that the Cu-NC-0–550 sample has a higher surface area than NC-decorated Cu-based samples, and further increasing the calcination temperature of NC-decorated Cu-based catalysts would lead to a gradual decrease in the specific surface area (**Table 2**), possibly owing to the surface coverage of the NC component and the agglomeration of particles, as further proven by the significantly reduced surface area of metallic copper obtained by N_2O titration (**Table 2**).

TEM images of reduced NC-decorated Cu-based samples obtained at different calcination temperatures are presented in **Fig. 2C** and **Fig. S6**. Among these samples, the Cu-NC-2–550 sample stands out due to its uniform dispersion of small Cu nanoparticles (NPs). Remarkably, the average size of Cu NPs, as estimated from TEM images, is found to be

Table 1

Comparison of different reference catalysts in the continuous upgrading of ethanol into higher alcohols.

Catalysts	Reaction conditions in fixed bed reactor	Conv. (%)	Select. ^a (%)	Yield. ^b (%)	R _{ethanol} ^c (mmol·g _{cat} ⁻¹ ·h ⁻¹)	STY ^d (mmol·g _{cat} ⁻¹ ·h ⁻¹)	Refs
MgO	450 °C, 0.1 MPa, W/F= 20.83 g·h·mol ⁻¹	56.0	32.8	18.4	26.8	8.8	[46]
Mg ₃ AlO _x	350 °C, 0.1 MPa, W/F= 23.33 g·h·mol ⁻¹	33.2	34.3	11.4	14.3	4.9	[47]
Sr-HAP	300 °C, 0.1 MPa, W/F= 130 g·h·mol ⁻¹	11.3	86.4	9.8	0.9	0.8	[48]
Cu/AlMgO-P	325 °C, 3.2 MPa, LHSV= 2.4 mL/(h·g _{cat})	23.3	48.8	11.4	9.6	4.7	[49]
Cu/HSACeO ₂	260 °C, 10 MPa, LHSV= 1.97 h ⁻¹	67	44.8	30.0	28.7	12.9	[14]
Cu-CeO ₂ /AC	250 °C, 2 MPa, LHSV= 2 h ⁻¹	45.6	42.4	19.3	31.8	13.5	[29]
Co-MgAlO _x	250 °C, 0.1 MPa, 0.96 g·g _{cat} ⁻¹ ·h ⁻¹	32.9	95.4	31.4	6.7	6.4	[43]
Ni-MgAlO _x	250 °C, 3 MPa, WHSV= 3.2 h ⁻¹	18.7	85	15.9	12.9	11.0	[31]
CuLaAlO _x	260 °C, 3 MPa, LHSV= 2 mL/(h·g _{cat})	52.5	72.7	38.2	17.7	12.9	[50]
NiO-Cu-LaAlO _x	250 °C, 3 MPa, LHSV= 2 mL/(h·g _{cat})	56.7	76.1	43.1	19.4	14.8	[51]
Ag/Mg ₂ AlO _x	350 °C, 0.1 MPa, LHSV= 6 mL/(h·g _{cat})	23.3	77.0	17.9	24.0	18.5	[52]
Pd@UiO-66	250 °C, 2 MPa, LHSV= 4 mL/(h·g _{cat})	49.9	50.1	25.0	34.2	17.2	[15]
Ru/Mg ₃ AlO _x	350 °C, 0.1 MPa, WHSV= 3.2 h ⁻¹	29.6	82.6	24.4	20.6	17.0	[33]
Cu-NiMgAl	250 °C, 3 MPa, WHSV= 1.69 h ⁻¹	30	64.2	19.3	11.0	7.1	[34]
Cu-NC-2-550	250 °C, 2 MPa, LHSV= 3.6 mL/(h·g _{cat})	63.0	82.0	51.7	38.9	31.9	This work

^a The products include n-BuOH, HexOH and OctOH.^b Yield represents the yield of higher alcohols.^c R represents the reaction rate of ethanol.^d STY represents the space time yield of higher alcohols.

approximately 2.0 nm, rather smaller than that of the Cu-NC-0-550 sample (5.2 nm). In accordance with the XRD results, the average size of Cu NPs gradually increases as the increased calcination temperature from 2.0 nm at 550 °C to 11.5 nm at 750 °C. It is seen that the average size of metallic copper particles for Cu-NC-2-550 estimated from the XRD line broadening of (111) plane is larger than that obtained from TEM images (Table 2), mainly due to the occurrence of strong interactions between Cu species and the support and thus the formation of a large number of small Cu⁰ particles with irregular shapes. Additionally, high-resolution TEM image of the Cu-NC-2-550 sample (Fig. 2D and Fig. 2E) reveals the presence of many small particles of 2.0 nm in size and a characteristic lattice with an interplanar distance of 0.209 nm in the enlarged region (inset in Fig. 2E), which agrees well with the (111) plane of metallic Cu crystallites. Moreover, the interplanar distance is 0.211 nm, associated with the (200) plane of the MgO phase. In addition, the HAADF-STEM image of the Cu-NC-2-550 sample (Fig. 2F-K) confirms the uniform dispersion of ultra-small Cu species on the support, along with the accumulation of N and C species on the surface. Additionally, elemental microanalysis reveals that compared to those in the synthesis mixture with a set melamine/Cu of 2.0, much less N and C elements were introduced into final Cu-NC-2-T catalysts (Table 2), due to the loss of melamine during the synthesis of melamine/CuMgAl-LDH composite precursors and the further loss of N and C elements during the subsequent calcination/reduction treatment. Especially, despite the same content of N as those in other Cu-NC-2 samples, Cu-NC-2-550 possesses smaller Cu⁰ NPs, probably due to the fact that the appropriate calcination temperature of 550 °C may be conducive to the formation of stronger interactions between Cu and NC species, thus inhibiting the aggregation and growth of Cu particles and leading to the generation of smaller Cu particles.

3.3. Surface-interface properties

XPS of different Cu-containing samples were obtained to identify the chemical states of N, C, Cu, and O species. As illustrated in Fig. 3A, in each case, three fitted peaks in the C 1 s spectra of Cu-based samples are assigned to the C-C bond (284.8 eV), C=N or C-O bond (285.8 eV), and C=O bond (289.2 eV) [55,56], respectively. As for Cu-NC-2-450 (Fig. S7), the N 1 s spectra show four deconvoluted peaks centered at approximately 398.3 eV, 399.3 eV, 400.0 eV, and 401.2 eV, which are assigned to pyridinic N species, pyrrolic N species, graphitic N species, and oxidized N species, respectively [56]. It is important to note that the low signal to noise ratio is mainly ascribed to the limited presence of N in the catalyst, which aligns with the N elemental analysis (Table 2).

In the fine Cu 2p spectra (Fig. 3B), there are two main peaks at about 933 and 942 eV, respectively, corresponding to Cu 2p_{3/2} and its satellites. After deconvolution, the spectrum shows two subpeaks at about 934.1 and 934.3 eV, which are associated with Cu²⁺ in CuO and Cu²⁺ species located in the MgAl₂O₄-like phase structure [57], respectively. Additionally, there is another peak at about 932.7 eV, which may be assigned to Cu⁰/Cu⁺ species [58], as further supported by the Cu LMM Auger spectra (Fig. 3 C). It is worth noting that Cu-NC samples exhibit a broad and asymmetrical Cu L₃M₄₅M₄₅ Auger spectrum, indicating the coexistence of Cu⁰, Cu²⁺, and Cu⁺ species [59–61]. For all catalysts, two characteristic peaks centered at the kinetic energy of 919.0 eV and 922.0 eV correspond to ¹G and ³F signals of the final 3d⁸ configuration, respectively, which arise from the L-S coupling of two 3d holes for Cu⁰. Furthermore, the peak at 912.7–913.5 eV can be attributed to 2 F*, which is the Auger vacancy satellite structure induced by the L₂L₃M₄₅ Coster-Kronig transition [62–64]. Noteworthy is the shift in kinetic energies of Cu species that indicates the enhanced interaction between copper and other components with the introduction of the NC component and the regulation of calcination temperature [65]. The Cu 2p_{3/2} peak shape for Cu-NC-0-550 and Cu-NC-2-450 samples is obviously different from those for other Cu-NC samples due to lower calcination temperatures and the difference in crystalline phase structure. According to Table 2, except for the Cu-NC-2-750 sample, the surface Cu⁺/Cu⁰ ratios on NC-decorated Cu-based samples are higher than that on the Cu-NC-0-550 sample, and the Cu-NC-2-550 sample has a higher surface Cu⁺/Cu⁰ ratio compared to other samples. These results unambiguously demonstrate that both surface NC modification and an appropriate calcination temperature can efficiently enhance Cu-support interactions, thereby facilitating the formation of Cu⁺ species at metal-support interfaces. It is suggested that these interfacial Cu⁺ sites function as active sites responsible for the adsorption and activation of ethoxide and carbonyl species formed during ethanol conversion.

Furthermore, in the O 1 s region of Cu-NC-0-550 sample, two main deconvoluted peaks are observed (Fig. 3D). The first peak (O_I, 530.2 eV) is correlated with lattice oxygen species, while the second peak (O_{II}, 531.4 eV) relates to the oxygen species adsorbed on surface defects, such as oxygen vacancies (O_V) [66]. As the calcination temperature increases, the O 1 s signals shift to lower binding energies. This suggests that both NC-modification and calcination temperature are imperative in regulating metal-support interactions. Melamine/LDH precursors undergo high temperature carbonization and subsequent reduction, which partially removes lattice oxygen atoms, resulting in the formation of defective Cu⁺-O_V-M or Mg-O_V-M structures (M=Mg, Al), consistent with the results of more Cu⁺ sites generated in Cu-NC catalysts. Notably, the

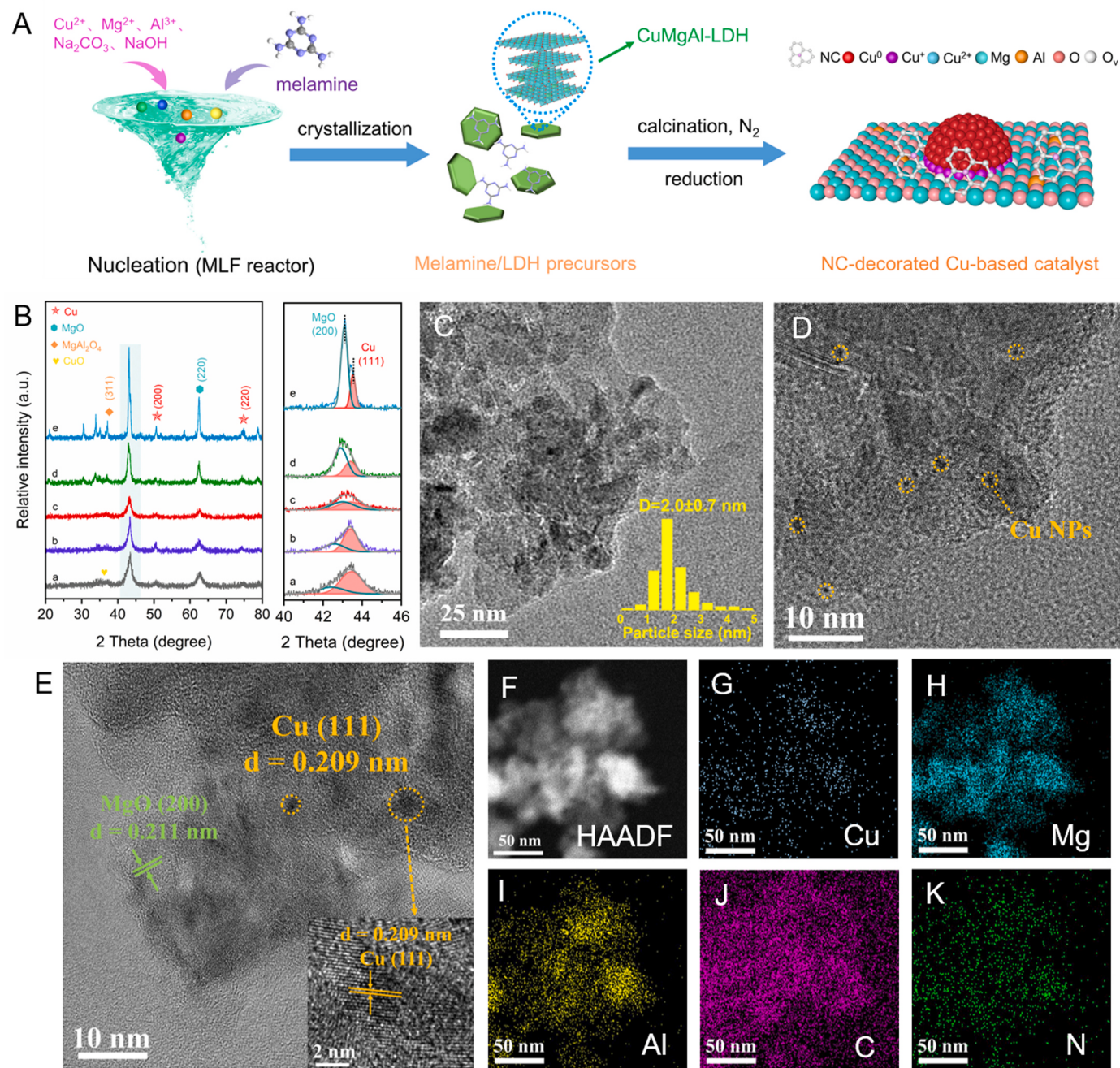


Fig. 2. (A) Schematic representation for the synthesis of the NC-decorated Cu-based samples; (B) XRD patterns of reduced samples: Cu-NC-0-550 (a), Cu-NC-2-450 (b), Cu-NC-2-550 (c), Cu-NC-2-650 (d), and Cu-NC-2-750 (e) in the 2θ ranges of $10\text{--}80^\circ$ and $40\text{--}46^\circ$, respectively; (C) TEM image with the histogram of size distribution of Cu-NC-2-550 sample; (D,E) HRTEM image of Cu-NC-2-550 sample, where yellow dashed circles represent small Cu particles; (F) HAADF-STEM image and EDS elemental-mapping analysis of (G) Cu, (H) Mg, (I) Al, (J) C, and (K) N elemental distributions for Cu-NC-2-550 sample.

Cu-NC-2-550 catalyst exhibits the highest O_{II}/O_I ratio of 0.47 (Fig. 3D), indicating more oxygen vacancies on its surface. It has previously been reported that oxygen vacancies may activate and stabilize acetaldehyde [67]. Therefore, the abundance of oxygen vacancies on NC-decorated copper catalysts can act as strong adsorption sites for acetaldehyde intermediate, effectively promoting subsequent condensation during ethanol conversion.

H_2 -TPD measurements were further performed to identify H_2 adsorption behaviors on Cu-based samples. As for the Cu-NC-0-550 presented in Fig. 3E, the desorption peaks below 500°C correspond to hydrogen chemically adsorbed at Cu^0 sites. The peaks in the range of $500\text{--}800^\circ\text{C}$ are typically relative to spillover hydrogen, which

originates from the dissociated hydrogen adsorbed on surface defects. It is worth noting that Cu-NC-2-550 exhibits a higher amount of spillover hydrogen compared to other Cu-based samples. This is mainly ascribed to the presence of more oxygen vacancies, which allows spillover hydrogen atoms to bond with them. However, as for the sample calcinated at 750°C , there is a substantial reduction in the amount of spillover hydrogen. This can be explained by the agglomeration of Cu NPs and the decrease in the number of defective structures. Moreover, as shown in Fig. 3F, in all cases, the broad signal in the EPR spectra ($g = 2.145\text{--}2.156$) is associated with oxygen vacancies with unpaired electrons, strongly supporting the existence of oxygen vacancies in Cu-based catalysts [68,69]. The ferromagnetic linewidth and the intensity of these

Table 2
Compositional and structural properties of different Cu-based catalysts.

Catalysts	Content (wt%)			S_{Cu}^{c} (m^2/g)	$S_{\text{BET}}^{\text{d}}$ (m^2/g)	$\text{Cu}^{+}/\text{Cu}^0$ ratio ^e	$D_{(111)}^{\text{f}}$ (nm)	$D_{\text{TEM}}^{\text{g}}$ (nm)
	Cu ^a	C ^b	N ^b					
Cu-NC-0-550	14.6	-	-	34.0	75	0.56	6.3	5.2
Cu-NC-2-450	13.1	2.76	0.06	17.6	57	0.78	10.1	6.2
Cu-NC-2-550	13.3	2.71	0.06	19.5	55	1.77	5.6	2.0
Cu-NC-2-650	13.4	1.90	0.05	19.5	36	0.78	11.6	6.4
Cu-NC-2-750	13.1	1.13	0.06	24.1	11	0.49	26.5	11.5

^a Determined by ICP-AES;

^b Determined by elemental microanalysis;

^c Active specific surface area of metallic copper determined by N_2O titration;

^d Specific surface area calculated by the BET method;

^e Calculated by Cu LMM XAES spectra;

^f Calculated by XRD patterns;

^g Determined by TEM images.

signals are associated with the density of vacancies, which follows the order:

Cu-NC-2-750 < CuNC-0-550 < Cu-NC-2-650 < Cu-NC-2-450 < Cu-NC-2-550, consistent with XPS of O 1 s and $\text{H}_2\text{-TPD}$ results. In addition, in

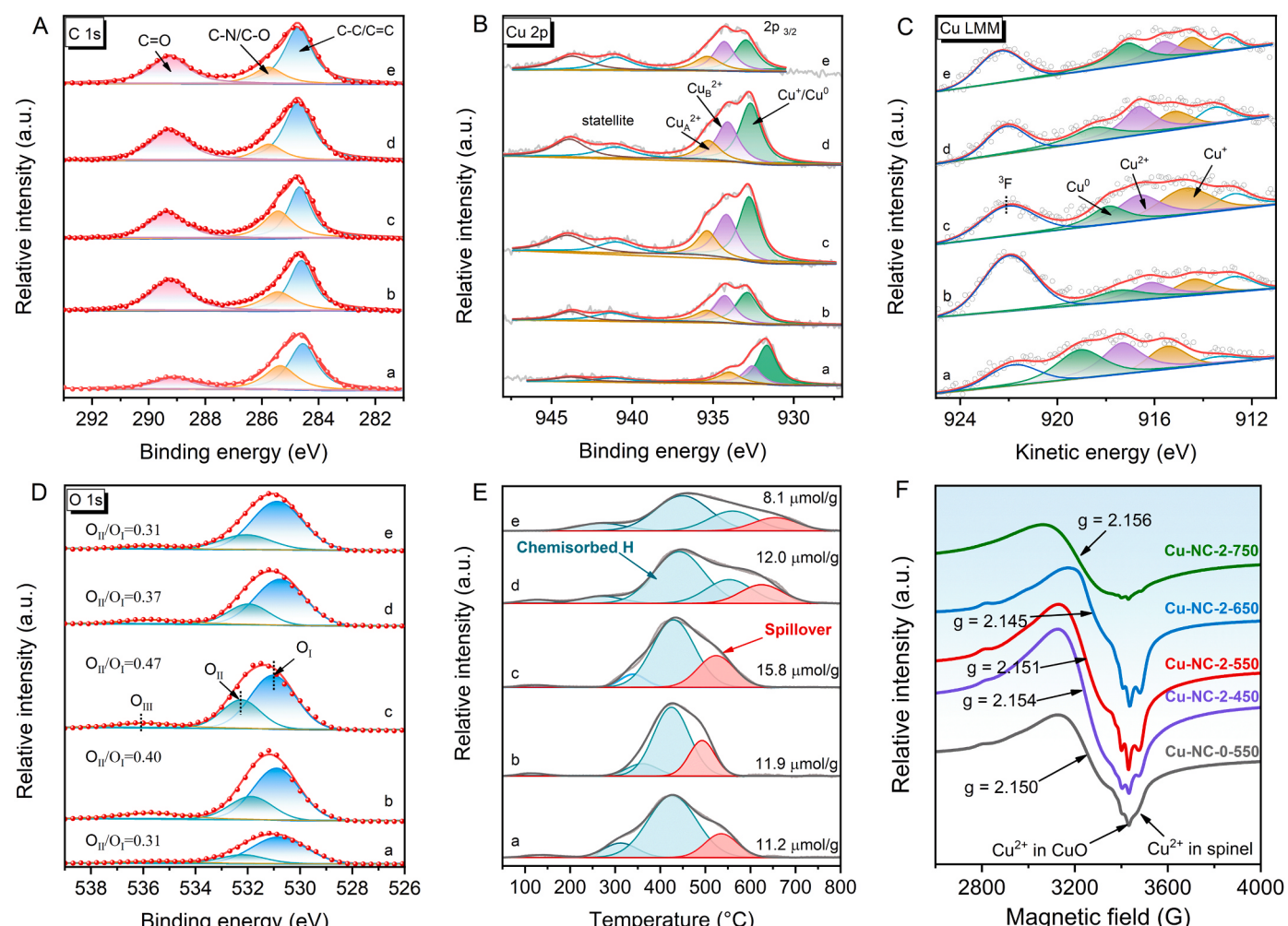


Fig. 3. (A) XPS of C 1s region, (B) XPS of Cu 2p region, (C) Cu LMM Auger spectra, and (D) XPS of O 1s region of Cu-based samples; (E) $\text{H}_2\text{-TPD}$ profiles of Cu-based samples; (F) EPR spectra of Cu-based samples: (a) Cu-NC-0-550, (b) Cu-NC-2-450, (c) Cu-NC-2-550, (d) Cu-NC-2-650, and (e) Cu-NC-2-750.

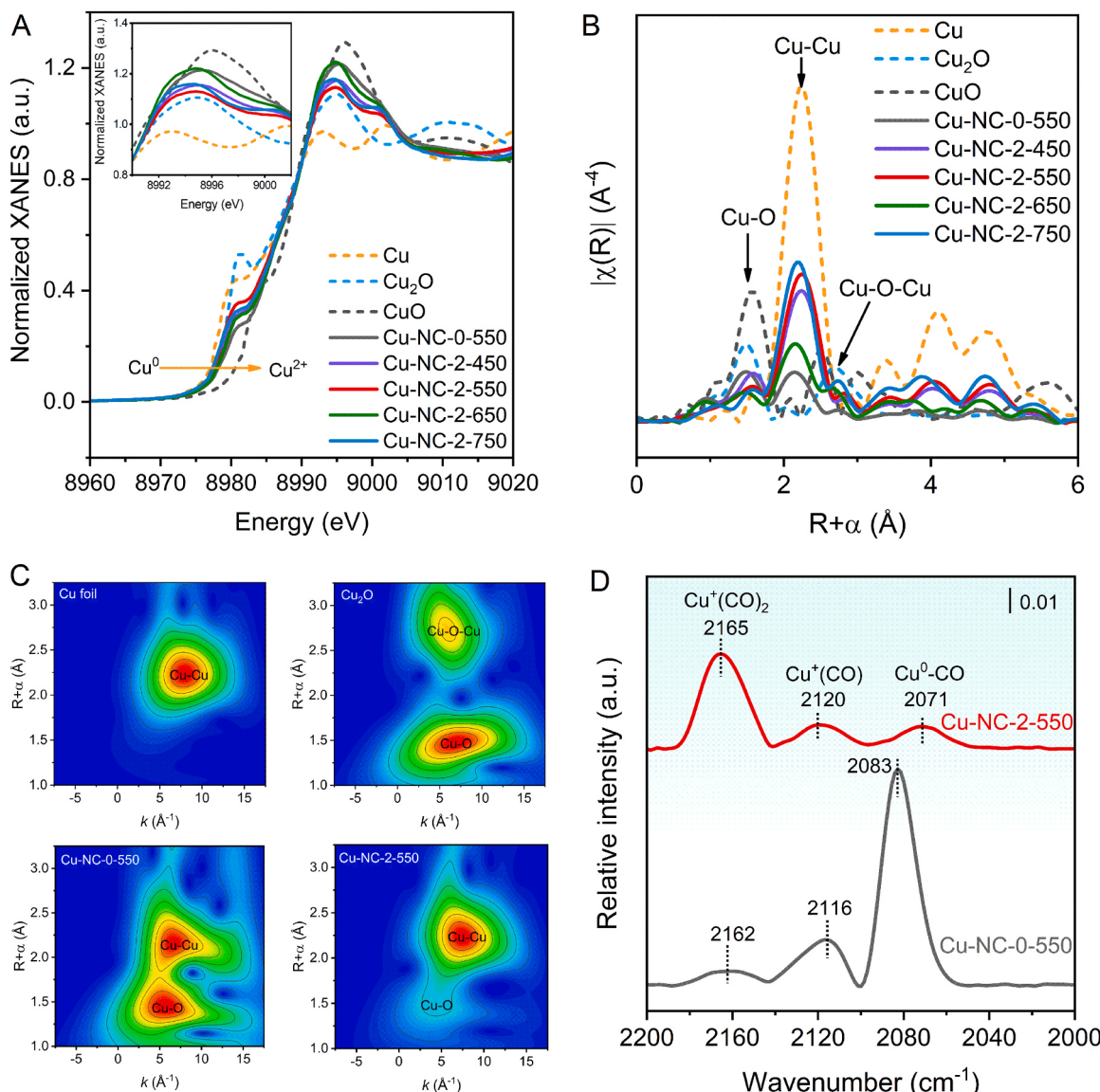


Fig. 4. (A) Normalized Cu K-edge XANES spectra and (B) corresponding Fourier transform k3-weighted Extended X-ray absorption fine structure (EXAFS) spectra in R space for NC-decorated Cu-based samples. (C) Wavelet transform for the EXAFS spectra of Cu foil, Cu₂O, Cu-NC-0-550, and Cu-NC-2-550 samples. (D) In situ CO-DRIFTS spectra of Cu-NC-0-550 (a) and Cu-NC-2-550 samples at 30 °C.

reaching a maximum of 20.9% in the Cu-NC-2-550 sample [71].

Furthermore, in order to disclose the surface structure of different Cu-containing catalysts, in-situ CO-DRIFT spectra were attained (Fig. 4D). After the purge of argon, two representative Cu-NC-0-550 and Cu-NC-2-550 samples present three characteristic peaks, which are associated with linearly adsorbed CO at Cu⁰ sites (2083/2071 cm⁻¹), adsorbed CO at Cu⁺ sites (2116 cm⁻¹), and adsorbed Cu^{+(CO)}₂ species (2162 cm⁻¹) [72]. Notably, compared to Cu-NC-0-550, the intensity of the two peaks related to CO adsorbed at Cu⁺ sites for Cu-NC-2-550 is significantly enhanced, while the peak of CO adsorbed at Cu⁰ sites is significantly reduced. This demonstrates the dominant existence of Cu⁺ species formed on the Cu-NC-2-550. Additionally, the band related to CO linearly adsorbed on Cu⁰ sites red-shifts from 2083 cm⁻¹ for Cu-NC-0-550 to 2071 cm⁻¹ for Cu-NC-2-550, which is attributable to the strengthened interactions between back-bonding of π*_{CO} orbitals and Cu d orbitals, indicative of the increased electron density of Cu⁰ sites. Such enhanced electron density of Cu⁰ sites may be related to the generation of considerable surface oxygen vacancies.

The concentration and strength of surface acidic and basic sites on catalysts are imperative in determining the selectivity of C-C coupling

products during ethanol upgrading. Therefore, NH₃-TPD and CO₂-TPD measurements were conducted to estimate surface acid-base strength and concentration of Cu-based samples. First, no obvious TCD signal in the TPDE curve of the representative Cu-NC-2-450 can be detected in the range of 50–500 °C (Fig. S9), demonstrating that CO₂-TPD or NH₃-TPD analysis of Cu-based catalysts may determine surface acid-base properties. According to the NH₃ desorption in the range of 50–500 °C (Fig. 5A), all samples exhibit three desorption regions (50–150 °C, 150–350 °C, and 350–500 °C, respectively), as a result of weak (A_w), medium-strength (A_{ms}), and strong acid (A_s) sites, respectively. The total amount of surface acid sites, especially weak sites, apparently decrease after the introduction of NC component in the samples (Fig. 5B and Table S3). Increasing the calcination temperature leads to a gradual decline in the number of acidic sites and alteration in the strength of acidic sites. The peaks associated with medium-strength acidic sites shift to a lower desorption temperature, indicating a reduction in the strength of acidic sites. Conversely, the strength of strong acidic sites increases with increasing calcination temperature, as evidenced by bands associated with strong acidic sites shifting to higher temperatures. Furthermore, the detailed information of surface Brønsted acid (BA) sites and

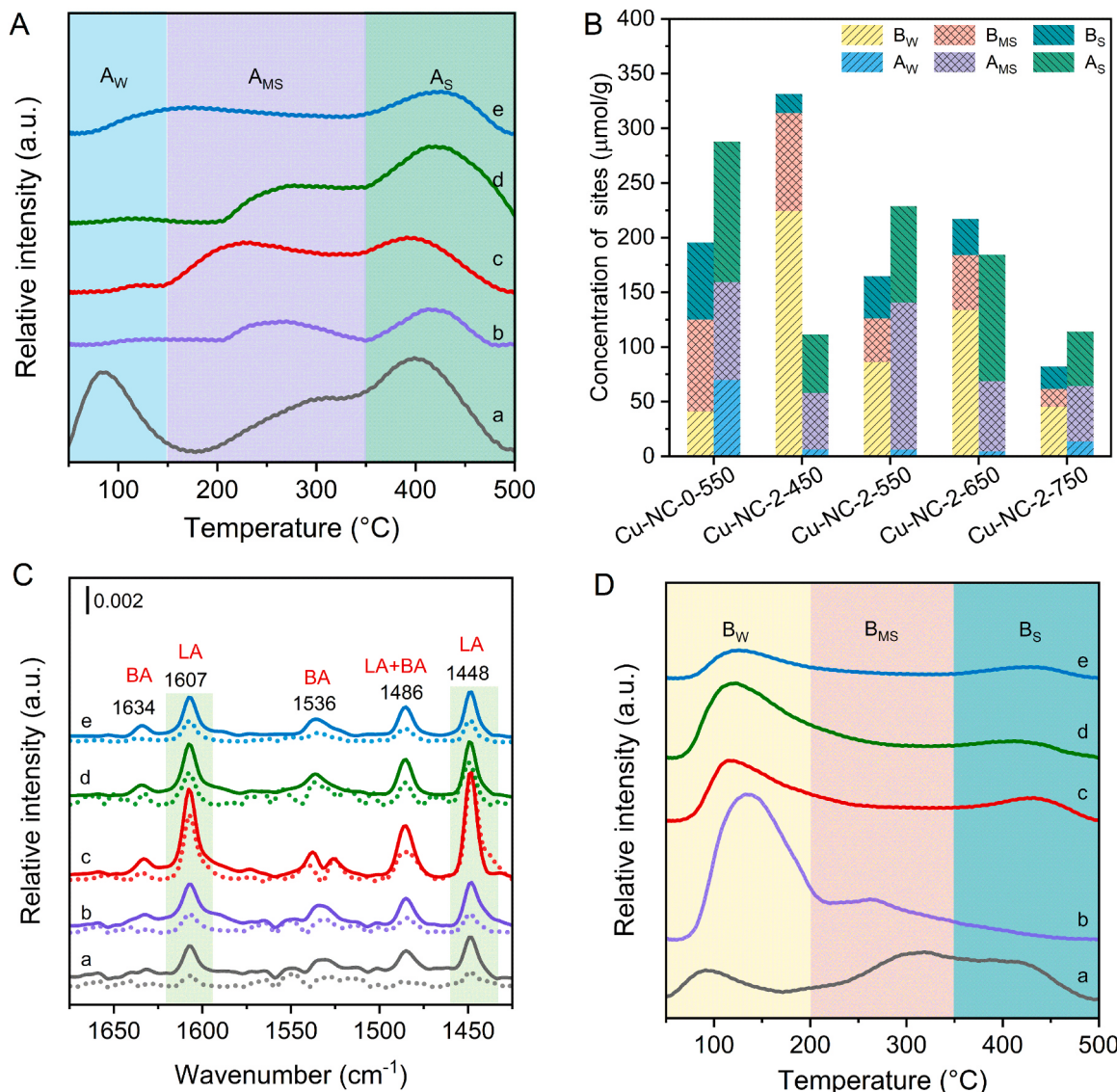


Fig. 5. (A) NH_3 -TPD profiles, (B) concentration of acid-base sites, (C) Pyridine-FTIR, and (D) CO_2 -TPD profiles for Cu-NC-0-550 (a), Cu-NC-2-450 (b), Cu-NC-2-550 (c), Cu-NC-2-650 (d), and Cu-NC-2-750 (e), respectively. The solid line in (D) represents the adsorption of pyridine at 50°C , while the dotted line represents the adsorption of pyridine at 200°C .

Lewis acid (LA) on the samples was elucidated using FT-IR spectroscopy of pyridine adsorption. As plotted in Fig. 5C, peaks at 1634 and 1536 cm^{-1} are attributable to pyridine adsorption at BA sites, and peaks at 1607 and 1448 cm^{-1} are reasonably assigned to pyridine binding to LA sites. Characteristic peaks at 1486 cm^{-1} are correlated with the combination of both LA and BA sites with pyridine. Notably, Cu-NC-2-550 exhibits a much higher intensity of LA sites than other samples, and the intensity of these acidic sites does not decrease significantly with increasing desorption temperature, indicating the presence of an abundance of strong LA sites on the Cu-NC-2-550 catalyst due to the contribution of plentiful Cu^+ species serving as LA sites [73]. Hence, it is suggested that an increase in strong LA sites on Cu-NC-2-550, as adsorption sites for ethanol, may enhance ethanol conversion. In addition, in the case of Cu-NC-2-550, pyridine bound to BA sites shows two split bands (1537 and 1525 cm^{-1}), indicative of the presence of two types of BA sites with different strength. Specifically, the presence of BA sites 1525 cm^{-1} indicates that BA acid sites become weaker [74], probably due to the formation of stronger interactions between amorphous alumina with surface hydroxyl groups and other species in the catalyst.

On the other hand, after surface NC modification, the basic properties of Cu-based samples undergo effective tuning, as observed in CO_2 -TPD profiles (Fig. 5D). In each case, CO_2 -TPD profiles can be categorized into three regions: $50\text{--}200^\circ\text{C}$, $200\text{--}350^\circ\text{C}$, and $350\text{--}500^\circ\text{C}$, which correspond to weak (B_W), medium-strength (B_{MS}), and strong (B_S) basic sites, respectively. Notably, surface NC modification leads to the formation of mass of weak basic sites (Fig. 5B and Table S3), as well as a significant reduction in the number of medium-strength or strong base sites, mainly owing to surface coverage of NC overlayer. As a result, more weak basic sites are provided and partial basic sites related to metal-oxygen pairs and lowly coordinated O^{2-} species on the catalyst surface are blocked.

Therefore, based on the above structural and catalytic reaction results, it can be concluded that surface NC component formed on Cu-based catalysts may interact strongly with Cu species or cover the partial surface of Cu NPs and the support, thereby significantly affecting the dispersion and chemical states of Cu species, Cu-support interfacial structures, and surface properties of the support and thus catalytic performance of catalysts.

3.4. Study on the mechanism for ethanol conversion

In order to account for the impact of surface NC modification on Cu-based catalysts on the absorption of reactants and intermediates, in situ DRIFT measurements of ethanol adsorption were conducted. As shown in Fig. 6A, the peaks at 1056 and 1074 cm⁻¹ represent the bidentate $\nu(C=O)$ band of ethoxide species on the Cu-NC-0-550. Furthermore, the monodentate $\nu(C=O)$ band appears at 1100 and 1117 cm⁻¹. It is worth noting that these bands decline dramatically with increasing the desorption temperature and vanish completely before 200 °C. When further elevated to 250 °C, a new $\nu(C=O)$ band of acetaldehyde adsorbed in η^1 conformation ($\eta^1\text{-AcH}$) appears at 1602 cm⁻¹ as a result of the dehydrogenation of ethanol, along with the $\nu(C=C)$ band of enolate intermediate formed at 1576 cm⁻¹. Furthermore, for the Cu-NC-2-550 catalyst (Fig. 6B), the characteristic band associated with $\eta^1\text{-AcH}$ emerges at lower temperature (200 °C). Additionally, the intensity of $\nu(C=O)$ band of acetaldehyde is significantly enhanced in comparison to that of Cu-NC-0-550 catalyst, indicating the more superior ethanol dehydrogenation activity of the catalyst with surface NC modification. To further elucidate the discrepancy in active sites and adsorption configuration of ethanol arising from surface NC modification, a comparative DFT calculation was performed using two models of Cu-MgO and NC-decorated Cu-MgO samples. As presented in the inset in

Fig. 6A, on the Cu-MgO model, the O atom of ethanol bonds to the Cu⁰ sites with 1.452 Å for the C-O bond length and -1.6 eV for the adsorption energy. In contrast, for the NC-decorated Cu-MgO model (Fig. 6C and inset in Fig. 6B), the O atom of ethanol coordinates with the Cu⁰ sites adjacent to NC with 1.455 Å for the C-O bond length and -2.54 eV for the adsorption energy. This further suggests that ethanol is more prone to adsorption on NC-decorated Cu-MgO via C-O bond, which coincides with the findings obtained by in situ DRIFT results of ethanol adsorption.

Surface NC modification endows NC-decorated Cu-based catalysts with more oxygen vacancies, which may promote acetaldehyde adsorption. As shown in Fig. 6D, over the Cu-NC-0-550, the $\nu(C=O)$ band of η^2 -adsorbed acetaldehyde can be detected at 1243 cm⁻¹. Additionally, the $\nu(C=O)$ band of crotonaldehyde or 3-hydroxybutanal formed by the aldol condensation appears at 1682 cm⁻¹. The stronger $\nu(C=O)$ band centered at 1725 cm⁻¹ is associated with η^1 -adsorbed acetaldehyde. These bands are also present on the Cu-NC-2-550, but the adsorption intensities differ from those observed on the Cu-NC-0-550, especially at higher temperatures. The adsorption of acetaldehyde ($\eta^1\text{-AcH}$) and crotonaldehyde on Cu-NC-2-550 is observed to be stronger at lower temperatures, and weaker at elevated temperature when compared with the Cu-NC-0-550 (Fig. 6E). To verify the promotion of surface oxygen vacancies on acetaldehyde adsorption, DFT calculations

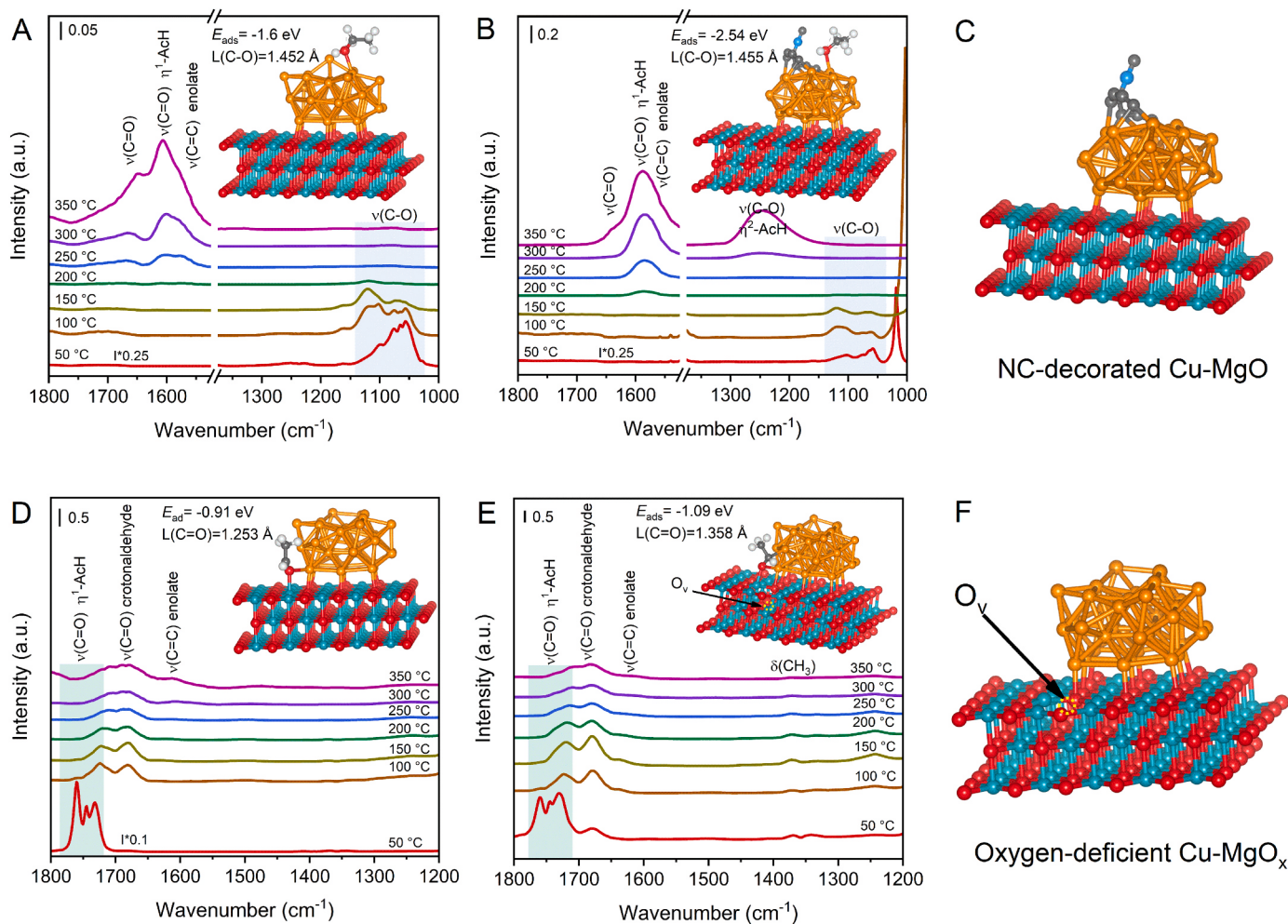


Fig. 6. In situ DRIFT spectra of ethanol adsorption over Cu-NC-0-550 (A) and Cu-NC-2-550 (B) at 50 °C, followed by desorption in the range of 50–350 °C. The structure of NC-decorated Cu-MgO model (C). In situ DRIFT spectra of acetaldehyde adsorption over Cu-NC-0-550 (D), and Cu-NC-2-550 (E), followed by desorption in the range of 50–350 °C. The structure of Cu-MgO_x model (F), where the yellow dotted circle represents one oxygen vacancy. The optimal adsorption structure of ethanol on Cu-MgO and NC-decorated Cu-MgO models are inserted in (A) and (B), respectively. The optimal adsorption structure of acetaldehyde at Cu-MgO and Cu-MgO_x model interfaces are inserted in (D) and (E), respectively.

were performed on Cu-MgO and Cu-MgO_x models (inset in Fig. 6D-E and Fig. 6F), which correspond to Cu supported on MgO and Cu supported on MgO containing one oxygen vacancy, respectively. Notably, the calculation results show that the C=O group of acetaldehyde binds to Cu⁺ and Mg²⁺ sites via O atom, where the C=O bond length is 1.253 Å and the adsorption energy is -0.91 eV. As for the Cu-MgO_x model, the O atom of acetaldehyde coordinates with interface Cu⁺ and surface Mg²⁺ sites adjacent to oxygen vacancies with 1.358 Å for the bond length of C=O and -1.09 eV for the adsorption energy, indicating that the C=O group of acetaldehyde is more prone to adsorb on sites adjacent to more oxygen vacancies. This observation suggests that surface NC modification can effectively enhance the adsorption strength of acetaldehyde intermediate.

To gain further insight into the roles of surface NC component on adsorption behaviors of the catalysts obtained at various calcination temperatures, in-situ DRIFT spectra of ethanol and acetaldehyde adsorption was attained at 250 °C (Fig. S10 and Fig. S11). Comparing catalysts obtained at different calcination temperatures, a significant difference in ethanol adsorption is observed, as evidenced by variations in the strength of characteristic bands related to ethoxide species, acetaldehyde, and coupling products. As depicted in Fig. S10, for Cu-NC-2-550, peaks denoting ν(C-O) and δ(CH₃) of ethoxide species, ν(OCO) of acetate, and ν(C=O) of acetaldehyde become increasingly stronger as the reaction time draws out. New peaks at 1732, 1744, and 1761 cm⁻¹ appear after ethanol adsorption for more than 20 min, indicating the presence of crotonaldehyde and 3-hydroxybutanal as condensation products. Notably, as for 450 °C and 750 °C calcined catalysts, weaker adsorption capacity strongly inhibits further C-C coupling, thus only forming a trace amount of acetaldehyde. Conversely, Cu-NC-2-650 promotes ethanol dehydrogenation, but the high surface affinity for acetaldehyde strongly blocks the desorption of the by-product, thus inhibiting subsequent condensation (Fig. S11). Based on the catalytic reaction and in-situ DRIFT results, proper adsorption/desorption ability of ethanol and reaction intermediates on Cu-NC-2-550 can promote selective conversion of ethanol and facilitate desorption of intermediates from dehydrogenation sites, thereby boosting catalytic performance.

As demonstrated above, surface NC modification intensifies the metal-support interaction, ensuring excellent durability for long-term reactions. This modification also exerts a profound influence on the remarkable activity of Cu-based catalysts through structural and electronic modification, resulting in enhanced activity for the production of higher alcohols. In combination with the experimental results and structural characterizations, several problems need to be discussed. The enhanced catalytic activity of Cu-NC-2-550 catalyst for upgrading ethanol to higher alcohols can be attributed to several factors.

Firstly, improved dehydrogenation activity plays a significant role, which is corroborated by both the Ea value for the whole reaction and the in-situ DRIFT of ethanol desorption. For Cu-NC-2-550 catalyst, the apparent activation energy for the whole Guerbet reaction decreases significantly compared to Cu-NC-0-550 catalyst, strongly suggesting that the surface NC component efficiently promotes ethanol activation and conversion. This promotion is mainly attributed to the highly dispersed smaller Cu NPs and thus the strong interactions between copper species and the support, which may favor the generation of more interfacial Cu⁺ sites and higher surface Cu⁰/Cu⁺ ratio [75–78], thus resulting in enhanced dehydrogenation, condensation, dehydration, and hydrogenation activities in the continuous conversion of ethanol to higher alcohols.

As for the continuous conversion of ethanol, both Cu⁰ and Cu⁺ have been reported to work in synergy. Predominantly, Cu⁰ sites are responsible for cleaving C-H and O-H bonds in the preliminary dehydrogenation reaction. On the other hand, electrophilic Cu⁺ sites serve as LA sites to polarize and stabilize ethoxide and carbonyl species [79–81]. Cu⁺ species can adsorb and activate the O-H bond in ethanol [82]. Additionally, Cu⁺ species serve as adsorption sites for ethoxy species.

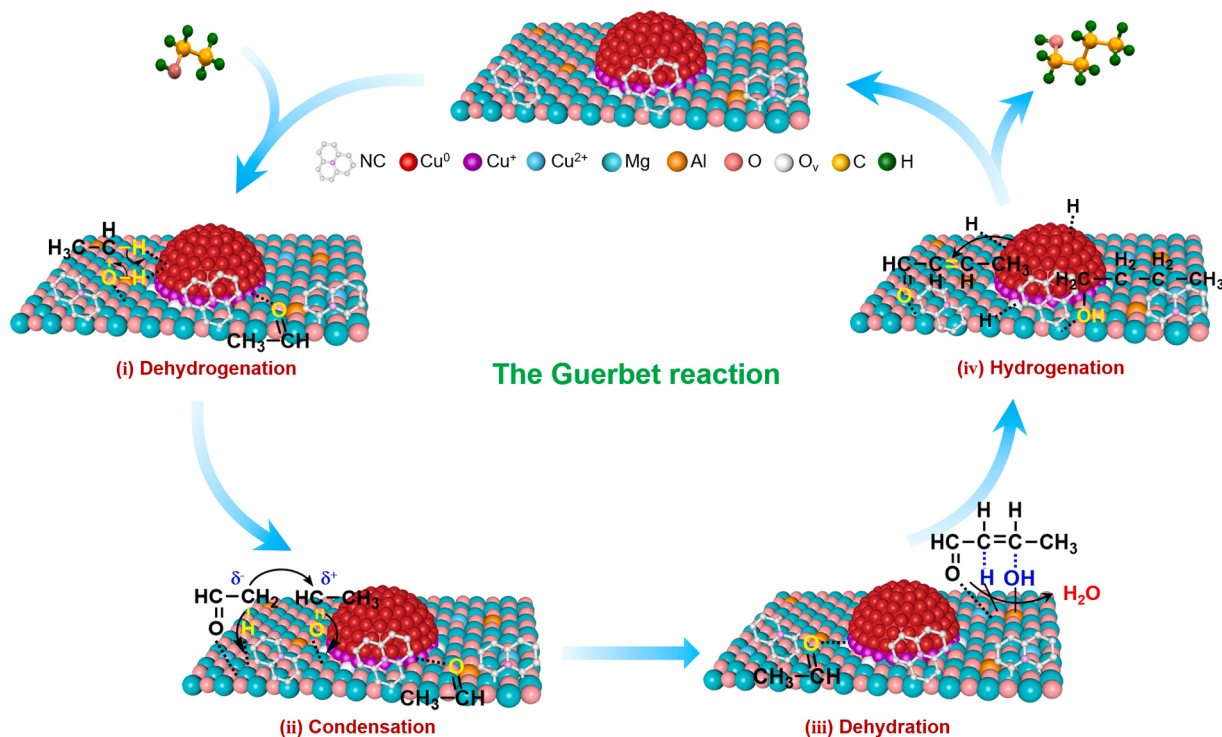
Accordingly, the dehydrogenation activity of ethanol depends largely on the synergistic effect between Cu⁰ and Cu⁺ [82]. In our case, surface Cu⁺/Cu⁰ ratio of Cu-NC-2-550 catalyst significantly increases compared to Cu-NC-0-550 catalyst, as shown above in situ CO-DRIFT and Cu LMM XAES results. Furthermore, pyridine-adsorption FTIR results reveal that the number of LA sites on Cu-NC-2-550, particularly strong LA sites, readily increases compared to Cu-NC-0-550 catalyst, primarily resulting from oxidized copper species. Consequently, a substantial difference in catalytic behavior in upgrading ethanol to higher alcohols may occur.

Secondly, the relationship between catalytic activity and Cu⁰ surface area (S_{Cu}) is not straightforward. Although Cu-NC-2-550 catalyst has a much lower S_{Cu} value than Cu-NC-0-550, the catalytic activity of Cu-NC-2-550 is higher, indicating that accessible Cu⁰ sites are not the only key prerequisite for superior activity. Intriguingly, a high proportion of Cu⁰ may promote hemiacetal hydrogenation and form ethyl acetate, whereas a sufficient surface population of Cu⁰ sites may increase the probability of hemiacetal dehydrogenation after nucleophilic addition of ethanol to acetaldehyde [83]. Therefore, Cu⁺/Cu⁰ sites promoting the C–H bond cleavage and H atoms transfer can play important and indispensable roles in upgrading ethanol to higher alcohols including n-butanol [82]. However, it is not necessary to have a high proportion of Cu⁰ for this process.

Thirdly, compared with Cu-NC-0-550 catalyst, Cu-NC-2-550 catalyst has a significantly reduced strength and number of both acidic and basic sites, due to surface NC modification. Acid-base properties typically lead to variations in product distributions over Cu-based catalysts with different calcination temperatures. For all Cu-based catalysts, the actual amount of amorphous alumina or MgO is approximate, due to the fixed Cu/Mg/Al molar ratio in the synthesis mixture. In all cases, amorphous alumina may mainly provide a smaller amount of surface LA sites, while MgO provides a larger number of surface basic sites. However, the strength and number of acidic or basic sites may be governed by the introduction of NC and calcination temperature, which is mainly attributed to the formation of interfacial Cu⁺ sites, as well as partial covering of acidic or basic sites by NC component and strong interactions between NC and alumina or MgO. Although ethanol and acetaldehyde intermediate can be adsorbed on acidic sites and adjacent base sites during the Guerbet reaction of ethanol, the total selectivity of higher alcohols remains constant at about 65%. Obviously, the number of acid-base sites alone does not correlate closely with selectivity to alcohols or esters, because interfacial Cu⁺ sites or oxygen vacancies as adsorption sites for ethanol and/or acetaldehyde are distinct factors determining selectivity, besides acidic and basic sites from alumina and MgO components. Therefore, surface NC modification and calcination temperature efficiently modify the surface-interface structures, which in turn affect the adsorption and activation of ethanol and acetaldehyde, ultimately governing the catalytic transformation of adsorbed species during the Guerbet reaction of ethanol.

As a result, surface NC modification can not only regulate adsorption mode and strength of reactants and intermediates, but also help disperse Cu NPs with smaller sizes, promote electron transfer, and alter oxidation states of copper species. Therefore, this modification gives rise to an appreciable activity for selective synthesis of higher alcohols from ethanol.

Considering the above results, a reasonable reaction mechanism over Cu-NC catalysts is proposed to explain the improvement of ethanol upgrading to n-butanol. As illustrated in Scheme 1, first, ethanol molecules are preferably adsorbed on surface LA sites (M^{δ+}: especially interfacial Cu⁺ sites) and adjacent base sites (O²⁻). This is followed by the hydrogen extraction from the α-C-H bond of adsorbed ethoxide species, thus promoting the generation of acetaldehyde with the participation of Cu⁰ species. Afterwards, carbonyl oxygen in one molecule of acetaldehyde may be adsorbed on the oxygen vacancy, while another molecule of acetaldehyde is adsorbed on LA sites and adjacent base sites. Subsequently, adsorbed acetaldehyde, after proton abstraction, forms a carbon anion intermediate that then reacts with another



Scheme 1. Proposed mechanism of the conversion of ethanol to n-butanol over the Cu-NC-2-550 catalyst.

adsorbed acetaldehyde, thereby generating the C-C coupling product through condensation reaction, with the cooperative effect of Cu^+ interfacial sites, oxygen vacancies, and acid-base sites. Next, the resulting crotonaldehyde intermediate undergoes dehydration and sequential hydrogenation to generate n-butanol. Therefore, compared to Cu-NC-0-550, Cu-NC-2-550 catalyst exhibits a superior activity in Guerbet reaction of ethanol and a lower apparent activation energy, which should be ascribed to the presence of multiple surficial-interfacial active sites including appropriate amount of Cu^0 sites, abundant interfacial Cu^+ sites, decreased number of acidic/basic sites, and more oxygen vacancies.

4. Conclusions

In summary, NC-decorated Cu-based catalysts were successfully synthesized via a melamine/CuMgAl-LDH composite precursor route and evaluated in upgrading ethanol to higher alcohols. As-constructed Cu-NC-2-550 catalyst with a 2:1 molar ratio of melamine/Cu in the precursor obtained at the calcination temperature of 550 °C exhibited a superior catalytic performance, along with a high selectivity to higher alcohols (82%) at high conversion of 63% under mild reaction conditions (250 °C, 2 MPa, and LHSV of 3.6 mL·g_{cat}⁻¹·h⁻¹). Remarkably, the catalyst achieved an unprecedented high production rate of higher alcohols (31.9 mmol·g_{cat}⁻¹·h⁻¹), which is the highest standard among previously reported catalysts to date. Comprehensive structural characterizations and DFT calculations revealed that surface NC modification on the catalyst surface improved the dispersion of Cu species and modulated surface acid-base properties, and facilitated the formation of interfacial Cu^+ sites and surface oxygen vacancies. Accordingly, favorable cooperative catalysis of multiple surface-interface active sites (Cu^0 , Cu^+ , oxygen vacancies, and acid-base sites) over the Cu-NC-2-550 catalyst remarkably boosted ethanol dehydrogenation and subsequent consecutive reactions including condensation, dehydration and hydrogenation processes. These results further indicate that introducing the appropriate amount of structural and electronic prompter, such as NC, is an effective approach for rationally designing high-performance

supported copper catalysts for efficient synthesis of higher alcohols from ethanol.

CRediT authorship contribution statement

Liyuan Yuan: Investigation, Writing – original draft. **Ming Zhang:** Visualization, Formal analysis. **Guoli Fan:** Methodology. **Feng Li:** Conceptualization, Writing – review & editing.

Declaration of Competing Interest

The authors declare that they have no known competing financial interests or personal relationships that could have appeared to influence the work reported in this paper.

Data availability

The authors do not have permission to share data.

Acknowledgements

This study was funded through National Natural Science Foundation of China (21991102; 22288102; U19B6002).

Appendix A. Supplementary data

Supplementary data associated with this article can be found, in the online version, at <https://doi.org/>.

Appendix A. Supporting information

Supplementary data associated with this article can be found in the online version at doi:[10.1016/j.apcatb.2023.123488](https://doi.org/10.1016/j.apcatb.2023.123488).

References

- [1] T. Zhang, Taking on all of the biomass for conversion, *Science* 367 (2020) 1305–1306.
- [2] C.R.V. Matheus, E.F. Sousa-Aguiar, Main catalytic challenges in ethanol chemistry, *A Rev., Cat. Rev. Sci. Eng.* (2022) 1–40.
- [3] J.Y. Zhang, E.J. Yoo, B.H. Davison, D.X. Liu, J.A. Schaidle, L. Tao, Z.L. Li, Towards cost-competitive middle distillate fuels from ethanol within a market-flexible biorefinery concept, *Green. Chem.* 23 (2021) 9534–9548.
- [4] C. Cesari, A. Gagliardi, A. Messori, N. Monti, V. Zanotti, S. Zucchini, I. Rivalta, F. Calcagno, C. Lucarelli, T. Tabanelli, F. Cavani, R. Mazzoni, Boosting the Guerbet reaction: a cooperative catalytic system for the efficient bio-ethanol refinery to second-generation biofuels, *J. Catal.* 405 (2022) 47–59.
- [5] H. Li, A. Riisager, S. Saravananurugan, A. Pandey, R.S. Sangwan, S. Yang, R. Luque, Carbon-increasing catalytic strategies for upgrading biomass into energy-intensive fuels and chemicals, *ACS Catal.* 8 (2018) 148–187.
- [6] S.M. Fu, Z.H. Shao, Y.J. Wang, Q. Liu, Manganese-catalyzed upgrading of ethanol into 1-butanol, *J. Am. Chem. Soc.* 139 (2017) 11941–11948.
- [7] J.F. Pang, M. Yin, P.F. Wu, X.Q. Li, H.Y. Li, M.Y. Zheng, T. Zhang, Advances in catalytic dehydrogenation of ethanol to acetaldehyde, *Green. Chem.* 23 (2021) 7902–7916.
- [8] L. Lin, P. Cao, J.F. Pang, Z.N. Wang, Q.K. Jiang, Y. Su, R. Chen, Z.J. Wu, M. Y. Zheng, W.H. Luo, Zeolite-encapsulated Cu nanoparticles with enhanced performance for ethanol dehydrogenation, *J. Catal.* 413 (2022) 565–574.
- [9] J.F. Pang, M.Y. Zheng, C. Wang, X.F. Yang, H. Liu, X.Y. Liu, J.M. Sun, Y. Wang, T. Zhang, Hierarchical echinus-like Cu-MFI catalysts for ethanol dehydrogenation, *ACS Catal.* 10 (2022) 13624–13629.
- [10] I. Ro, Y.F. Liu, M.R. Ball, D.H.K. Jackson, J.P. Chada, C. Sener, T.F. Kuech, R. J. Madon, G.W. Huber, J.A. Dumesic, Role of the Cu-ZrO₂ interfacial sites for conversion of ethanol to ethyl acetate and synthesis of methanol from CO₂ and H₂, *ACS Catal.* 6 (2016) 7040–7050.
- [11] J.Y. Zhang, E.C. Wegener, N.R. Samad, J.W. Harris, K.A. Unocic, L.F. Allard, S. Purdy, S. Adhikari, M.J. Cordon, J.T. Miller, T.R. Krause, S.C. Cheng, D.X. Liu, M.J. Li, X. Jiang, Z.L. Wu, Z.L. Li, Isolated metal sites in Cu-Zn-Y/Beta for direct and selective butene-rich C₄₊ olefin formation from ethanol, *ACS Catal.* 11 (2021) 9885–9897.
- [12] L.L. Xu, R.R. Zhao, W.P. Zhang, One-step high-yield production of renewable propene from bioethanol over composite ZnCeOx oxide and HBeta zeolite with balanced Brønsted/Lewis acidity, *Appl. Catal. B: Environ.* 279 (2020), 119389.
- [13] L. Qi, Y.F. Zhang, M.A. Conrad, C.K. Russell, J. Miller, A.T. Bell, Ethanol conversion to butadiene over isolated zinc and yttrium sites grafted onto dealuminated beta zeolite, *J. Am. Chem. Soc.* 142 (2020) 14674–14687.
- [14] J.H. Earley, R.A. Bourne, M.J. Watson, M. Poliakoff, Continuous catalytic upgrading of ethanol to n-butanol and >C₄ products over Cu/CeO₂ catalysts in supercritical CO₂, *Green. Chem.* 17 (2015) 3018–3025.
- [15] D.H. Jiang, G.Q. Fang, Y.Q. Tong, X.Y. Wu, Y.F. Wang, D.S. Hong, W.H. Leng, Z. Liang, P.X. Tu, L. Liu, K.Y. Xu, J. Ni, X.N. Li, Multifunctional Pd@UiO-66 catalysts for continuous catalytic upgrading of ethanol to n-butanol, *ACS Catal.* 8 (2018) 11973–11978.
- [16] D. Kiani, J. Baltrusaitis, Surface chemistry of hydroxyapatite for sustainable n-butanol production from bio-ethanol, *Chem. Catal.* 1 (2021) 782–801.
- [17] A. Galadima, O. Muraza, Catalytic upgrading of bioethanol to fuel grade biobutanol: a review, *Ind. Eng. Chem. Res.* 54 (2015) 7181–7194.
- [18] J.T. Kozlowski, R.J. Davis, Heterogeneous catalysts for the Guerbet coupling of alcohols, *ACS Catal.* 3 (2013) 1588–1600.
- [19] X.Y. Wu, G.Q. Fang, Y.Q. Tong, D.H. Jiang, Z. Liang, W.H. Leng, L. Liu, P.X. Tu, H. J. Wang, J. Ni, X.N. Li, Catalytic upgrading of ethanol to n-butanol: progress in catalyst development, *ChemSusChem* 11 (2018) 71–85.
- [20] F. Zaccheria, N. Scotti, N. Ravasio, The role of copper in the upgrading of bioalcohols, *ChemCatChem* 10 (2018) 1526–1535.
- [21] O.V. Larina, K.V. Valihura, P.I. Kyriienko, N.V. Vlasenko, D.Y. Balakin, I. Khalakan, T. Ćendak, S.O. Soloviev, S.M. Orlyk, Successive vapour phase Guerbet condensation of ethanol and 1-butanol over Mg-Al oxide catalysts in a flow reactor, *Appl. Catal. A: Gen.* 588 (2019), 117265.
- [22] J.A. Barrett, Z.R. Jones, C. Stickelmaier, N. Schopp, P.C. Ford, A pinch of salt improves n-butanol selectivity in the Guerbet condensation of ethanol over Cu-doped Mg/Al oxides, *ACS Sus. Chem. Eng.* 6 (2018) 15119–15126.
- [23] L. Faba, J. Cueto, M.Á. Portillo, Á.L. Villanueva Perales, S. Ordóñez, F. Vidal-Barbero, Effect of catalyst surface chemistry and metal promotion on the liquid-phase ethanol condensation to higher alcohols, *Appl. Catal. A: Gen.* 643 (2022), 118783.
- [24] Q.N. Wang, B.C. Zhou, X.F. Weng, S.P. Lv, F. Schüth, A.H. Lu, Hydroxyapatite nanowires rich in [Ca–O–P] sites for ethanol direct coupling showing high C_{6–12} alcohol yield, *Chem. Commun.* 55 (2019) 10420–10423.
- [25] T. Moteki, D.W. Flaherty, Mechanistic insight to C–C bond formation and predictive models for cascade reactions among alcohols on Ca-and Sr-hydroxyapatites, *ACS Catal.* 6 (2016) 4170–4183.
- [26] T. Riiutonen, K. Eränen, P. Mäki-Arvela, A. Shchukarev, A.R. Rautio, K. Kordas, N. Kumar, T. Salmi, J.P. Mikkola, Continuous liquid-phase valorization of bio-ethanol towards bio-butanol over metal modified alumina, *Renew. Energy* 74 (2015) 369–378.
- [27] B.C. Zhou, W.C. Li, W.L. Lv, S.Y. Xiang, X.Q. Gao, A.H. Lu, Enhancing ethanol coupling to produce higher alcohols by tuning H₂ partial pressure over a copper-hydroxyapatite catalyst, *ACS Catal.* 12 (2022) 12045–12054.
- [28] M.F. Guo, M.J. Gray, H. Job, C. Alvarez-Vasco, S. Subramaniam, X. Zhang, L. Kovarik, V. Murugesan, S. Phillips, K.K. Ramasamy, Uncovering the active sites and demonstrating stable catalyst for the cost-effective conversion of ethanol to 1-butanol, *Green. Chem.* 23 (2021) 8030–8039.
- [29] D.H. Jiang, X.Y. Wu, J. Mao, J. Ni, X.N. Li, Continuous catalytic upgrading of ethanol to n-butanol over Cu–CeO₂/AC catalysts, *Chem. Commun.* 52 (2016) 13749–13752.
- [30] P.A. Cuello-Penalosa, R.G. Dastidar, S.C. Wang, Y. Du, M.P. Lanci, B. Wooler, C. E. Kliewer, I. Hermans, J.A. Dumesic, G.W. Huber, Ethanol to distillate-range molecules using Cu/Mg_xAl_yO_z catalysts with low Cu loadings, *Appl. Catal. B: Environ.* 304 (2022), 120984.
- [31] J.F. Pang, M.Y. Zheng, L. He, L. Li, X.L. Pan, A.Q. Wang, X.D. Wang, T. Zhang, Upgrading ethanol to n-butanol over highly dispersed Ni–MgAlO catalysts, *J. Catal.* 344 (2016) 184–193.
- [32] Q.N. Wang, X.F. Weng, B.C. Zhou, S.P. Lv, S. Miao, D.L. Zhang, Y. Han, S.L. Scott, F. Schüth, A.H. Lu, Direct, selective production of aromatic alcohols from ethanol using a tailored bifunctional cobalt–hydroxyapatite catalyst, *ACS Catal.* 9 (2019) 7204–7216.
- [33] B.W. Yuan, J. Zhang, Z. An, Y.R. Zhu, X. Shu, H.Y. Song, X. Xiang, W.N. Wang, Y. S. Jing, L.R. Zheng, J. He, Atomic Ru catalysis for ethanol coupling to C₄₊ alcohols, *Appl. Catal. B: Environ.* 309 (2022), 121271.
- [34] Z.N. Wang, M. Yin, J.F. Pang, X.Q. Li, Y.N. Xing, Y. Su, S.M. Liu, X.Y. Liu, P.F. Wu, M.Y. Zheng, T. Zhang, Active and stable Cu doped NiMgAlO catalysts for upgrading ethanol to n-butanol, *J. Energy Chem.* 72 (2022) 306–317.
- [35] Z. Gao, C.Y. Li, G.L. Fan, L. Yang, F. Li, Nitrogen-doped carbon-decorated copper catalyst for highly efficient transfer hydrogenolysis of 5-hydroxymethylfurfural to convertibly produce 2, 5-dimethylfuran or 2, 5-dimethyltetrahydrofuran, *Appl. Catal. B: Environ.* 226 (2018) 523–533.
- [36] F.J. Lan, H.L. Zhang, C.Y. Zhao, Y. Shu, Q.X. Guan, W. Li, Copper clusters encapsulated in carbonaceous mesoporous silica nanospheres for the valorization of biomass-derived molecules, *ACS Catal.* 12 (2022) 5711–5725.
- [37] S.F. Liu, W. Xu, Y.M. Niu, B.S. Zhang, L.R. Zheng, W. Liu, L. Li, J.H. Wang, Ultrastable Au nanoparticles on titania through an encapsulation strategy under oxidative atmosphere, *Nat. Commun.* 10 (2019) 1–9.
- [38] Q. Hu, L. Yang, G.L. Fan, F. Li, Hydrogenation of biomass-derived compounds containing a carbonyl group over a copper-based nanocatalyst: Insight into the origin and influence of surface oxygen vacancies, *J. Catal.* 340 (2016) 184–195.
- [39] G. Kresse, J. Furthmüller, Efficient iterative schemes for ab initio total-energy calculations using a plane-wave basis set, *Phys. Rev. B* 54 (1996) 11169.
- [40] P.E. Blöchl, Projector augmented-wave method, *Phys. Rev. B* 50 (1994) 17953–17979, 17953.
- [41] J.P. Perdew, K. Burke, M. Ernzerhof, Generalized gradient approximation made simple, *Phys. Rev. Lett.* 77 (1996) 3865.
- [42] S. Grimme, J. Antony, S. Ehrlich, H. Krieg, A consistent and accurate ab initio parametrization of density functional dispersion correction (DFT-D) for the 94 elements H–Pu, *J. Chem. Phys.* 132 (2010), 154104.
- [43] W.L. Lv, L. He, W.C. Li, B.C. Zhou, S.P. Lv, A.H. Lu, Atomically dispersed Co²⁺ on MgAlOx boosting C_{4–10} alcohols selectivity of ethanol valorization, *Green. Chem.* 25 (2023) 2653–2662.
- [44] X. Lin, X. Fei, D. Chen, Y. Qi, Q. Xu, Y. Liu, Q. Zhang, S. Li, T. Wang, Y. Qin, X. Qiu, Efficient catalytic upgrading of ethanol to higher alcohols via inhibiting C–C cleavage and promoting C–C coupling over biomass-derived NiZn@NC catalysts, *ACS Catal.* 12 (2022) 11573–11585.
- [45] B. Liu, H.-Q. Peng, J. Cheng, K. Zhang, D. Chen, D. Shen, S. Wu, T. Jiao, X. Kong, Q. Gao, S. Bu, C.-S. Lee, W. Zhang, Nitrogen-doped graphene-encapsulated nickel–copper alloy nanoflower for highly efficient electrochemical hydrogen evolution reaction, *Small* 15 (2019) 1901545.
- [46] A.S. Ndou, N. Plint, N.J. Coville, Dimerisation of ethanol to butanol over solid-base, *Appl. Catal. A: Gen.* 251 (2003) 337–345.
- [47] D.L. Carvalho, R.R. de Avillez, M.T. Rodrigues, L.E.P. Borges, L.G. Appel, Mg and Al mixed oxides and the synthesis of n-butanol from ethanol, *Appl. Catal. A: Gen.* 415 (2012) 96–100.
- [48] S. Ogo, A. Onda, Y. Iwasa, K. Hara, A. Fukuoka, K. Yanagisawa, 1-Butanol synthesis from ethanol over strontium phosphate hydroxyapatite catalysts with various Sr/P ratios, *J. Catal.* 296 (2012) 24–30.
- [49] D.D. Petrolini, N. Eagan, M.R. Ball, S.P. Burt, I. Hermans, G.W. Huber, J. A. Dumesic, L. Martins, Ethanol condensation at elevated pressure over copper on AlMgO and AlCaO porous mixed-oxide supports, *Catal. Sci. Technol.* 9 (2019) 2032–2042.
- [50] H.J. Zhao, X.Y. Shen, J.F. He, J.Y. Kou, T.J. Tao, Y. Can, H. Huang, D.H. Jiang, L. L. Lin, X.N. Li, Catalytic upgrading of ethanol to higher alcohols over ordered mesoporous Cu-La-Al composite metal oxides, *Appl. Surf. Sci.* 599 (2022), 153851.
- [51] J.F. He, X.Z. Li, J.Y. Kou, T.J. Tao, X.Y. Shen, D.H. Jiang, L.L. Lin, X.N. Li, Catalytic upgrading of ethanol to higher alcohols over nickel-modified Cu-La₂O₃/Al₂O₃ Catalysts, *Catal. Sci. Technol.* 13 (2022) 170–177.
- [52] J. Zhang, K. Shi, Z. An, Y.R. Zhu, X. Shu, H.Y. Song, X. Xiang, J. He, Acid–base promoted dehydrogenation coupling of ethanol on supported Ag particles, *Ind. Eng. Chem. Res.* 59 (2020) 3342–3350.
- [53] R. Shi, F. Wang, X. Mu, N. Ta, Y. Li, X. Huang, W. Shen, Transfer dehydrogenation of 1-octanol to 1-octanal over Cu/MgO catalyst: Effect of Cu particle size, *Chin. J. Catal.* 31 (2010) 626–630.
- [54] T. Zhang, B. Yuan, W. Wang, J. He, X. Xiang, Tailoring ³H intermediate coverage on the CuAl₂O₄/CuO catalyst for enhanced electrocatalytic CO₂ reduction to ethanol, *Angew. Chem. Int. Ed.* (2023), e2022096.
- [55] W.J. Yuan, S.P. Zhang, Y.Y. Wu, X.M. Huang, F.H. Tian, S.W. Liu, C.H. Li, Enhancing the room-temperature catalytic degradation of formaldehyde through constructing surface lewis pairs on carbon-based catalyst, *Appl. Catal. B: Environ.* 272 (2020), 118992.

- [56] J.P. Hong, B. Wang, G.Q. Xiao, N. Wang, Y.H. Zhang, A.Y. Khodakov, J.L. Li, Tuning the metal-support interaction and enhancing the stability of titania-supported cobalt Fischer-Tropsch catalysts via carbon nitride coating, *ACS Catal.* 10 (2020) 5554–5566.
- [57] K. Sun, M.H. Tan, Y.X. Bai, X.F. Gao, P. Wang, N.N. Gong, T. Zhang, G.H. Yang, Y. S. Tan, Design and synthesis of spherical-platelike ternary copper-cobalt-manganese catalysts for direct conversion of syngas to ethanol and higher alcohols, *J. Catal.* 378 (2019) 1–16.
- [58] J. Wu, G. Gao, P. Sun, X.D. Long, F.W. Li, Synergetic catalysis of bimetallic CuCo nanocomposites for selective hydrogenation of bioderived esters, *ACS Catal.* 7 (2017) 7890–7901.
- [59] J.P. Espinós, J. Morales, A. Barranco, A. Caballero, J.P. Holgado, A.R. González-Elipe, Interface effects for Cu, CuO, and Cu₂O deposited on SiO₂ and ZrO₂. XPS determination of the valence state of copper in Cu/SiO₂ and Cu/ZrO₂ catalysts, *J. Phys. Chem. B*, 106 (2002) 6921–6929.
- [60] M.C. Biesinger, Advanced analysis of copper X-ray photoelectron spectra, *Surf. Interface Anal.* 49 (2017) 1325–1334.
- [61] S. Pouston, P.M. Parlett, P. Stone, M. Bowker, Surface oxidation and reduction of CuO and Cu₂O studied using XPS and XAES, *Surf. Interface Anal.* 24 (2015) 811–820.
- [62] J.F. Yu, X.T. Sun, X. Tong, J.X. Zhang, J. Li, S.Y. Li, Y.F. Liu, N. Tsubaki, T. Abe, J. Sun, Ultra-high thermal stability of sputtering reconstructed Cu-based catalysts, *Nat. Commun.* 12 (2021) 7209.
- [63] W. Zhang, C.Q. Huang, Q. Xiao, L. Yu, L. Shuai, P.F. An, J. Zhang, M. Qiu, Z.F. Ren, Y. Yu, Atypical oxygen-bearing copper boosts ethylene selectivity toward electrocatalytic CO₂ reduction, *J. Am. Chem. Soc.* 142 (2020) 11417–11427.
- [64] L. Zhang, J.F. Yu, X.T. Sun, J. Sun, Engineering nanointerfaces of Cu-based catalysts for balancing activity and stability of reverse water-gas-shift reaction, *J. CO₂ Util.* 71 (2023), 102460.
- [65] W. Li, G.L. Fan, L. Yang, F. Li, Highly efficient synchronized production of phenol and 2,5-dimethylfuran through a bimetallic Ni–Cu catalyzed dehydrogenation–hydrogenation coupling process without any external hydrogen and oxygen supply, *Green. Chem.* 19 (2017) 4353–4363.
- [66] M.R. Liu, J.Y. Zhang, L.R. Zheng, G.L. Fan, L. Yang, F. Li, Significant promotion of surface oxygen vacancies on bimetallic CoNi nanocatalysts for hydrodeoxygenation of biomass-derived vanillin to produce methylcyclohexanol, *ACS Sus. Chem. Eng.* 8 (2020) 6075–6089.
- [67] Z. Liang, D.H. Jiang, G.Q. Fang, W.H. Leng, P.X. Tu, Y.Q. Tong, L. Liu, J. Ni, X. N. Li, Catalytic enhancement of aldol condensation by oxygen vacancy on CeO₂ catalysts, *ChemistrySelect* 4 (2019) 4364–4370.
- [68] O. Martín, A.J. Martín, C. Mondelli, S. Mitchell, T.F. Segawa, R. Hauer, C. Drouilly, D. Curulla-Ferré, J. Pérez-Ramírez, Indium oxide as a superior catalyst for methanol synthesis by CO₂ hydrogenation, *Angew. Chem. Int. Ed.* 55 (2016) 6261–6265.
- [69] T. Pinheiro Araújo, C. Mondelli, M. Agrachev, T.S. Zou, P.O. Willi, K.M. Engel, R. N. Grass, W.J. Stark, O.V. Safonova, G. Jeschke, S. Mitchell, J. Pérez-Ramírez, Flame-made ternary Pd-In₂O₃-ZrO₂ catalyst with enhanced oxygen vacancy generation for CO₂ hydrogenation to methanol, *Nat. Commun.* 13 (2022) 5610.
- [70] H.B. Zhao, R.F. Yu, S.C. Ma, K.Z. Xu, Y. Chen, K. Jiang, Y. Fang, C.X. Zhu, X.C. Liu, Y. Tang, L.Z. Wu, Y.Q. Wu, Q.K. Jiang, P. He, Z.P. Liu, L. Tan, The role of Cu₁–O₃ species in single-atom Cu/ZrO₂ catalyst for CO₂ hydrogenation, *Nat. Catal.* 5 (2022) 818–831.
- [71] R.O. Yang, J.Y. Duan, P.P. Dong, Q.L. Wen, M. Wu, Y.W. Liu, Y. Liu, H.Q. Li, T. Y. Zhai, In situ Halogen-Ion leaching regulates multiple sites on tandem catalysts for efficient CO₂ electroreduction to C₂₊ products, *Angew. Chem. Int. Ed.* 61 (2022), e202116706.
- [72] Q. Xu, C.G. Wang, Z.L. Shang, C. Zhang, X.C. Wang, Q. Liu, L.L. Dang, Y.C. Liu, F. Y. Zhao, Hydrogenation of biomass lactones to diols over CuLa_x/γ-Al₂O₃ catalyst: the promoting role of LaO_x, *Appl. Catal. B: Environ.* 317 (2022), 121689.
- [73] X. Li, J. Pang, Y. Zhao, P. Wu, W. Yu, P. Yan, Y. Su, M. Zheng, Ethanol dehydrogenation to acetaldehyde over a Cu⁸⁺-based Cu-MFI catalyst, *Chin. J. Catal.* 49 (2023) 91–101.
- [74] Z.-Q. Li, X. Fu, C. Gao, J. Huang, B. Li, Y. Yang, J. Gao, Y. Shen, Z. Peng, J.-H. Yang, Z. Liu, Enhancing the matching of acid/metal balance by engineering an extra Si-Al framework outside the Pd/HBeta catalyst towards benzene hydroalkylation, *Catal. Sci. Technol.* 10 (2020) 1467–1476.
- [75] Y. Fang, H. Sun, W. Peng, Q.H. Yuan, C. Zhao, Effect of surface [Cu₄O] moieties on the activity of Cu-based catalysts, *ACS Catal.* 12 (2022) 5162–5173.
- [76] E.X. Yuan, P. Ni, J. Xie, P.M. Jian, X. Hou, Highly efficient dehydrogenation of 2,3-butanediol induced by metal-support interface over Cu-SiO₂ catalysts, *ACS Sus. Chem. Eng.* 8 (2020) 15716–15731.
- [77] J. Zhang, Y.Z. Zhang, J.Q. Zhao, Z. An, Y.R. Zhu, X. Shu, H.Y. Song, X. Xiang, X. D. Ma, J. He, Cu-Pd pair facilitated simultaneous activation of ethanol and CO, *J. Catal.* 386 (2020) 81–93.
- [78] J.F. Yu, M. Yang, J.X. Zhang, Q.J. Ge, A.N. Zimina, T. Pruessmann, L. Zheng, J. D. Grunwaldt, J. Sun, Stabilizing Cu⁺ in Cu/SiO₂ catalysts with a shattuckite-like structure boosts CO₂ hydrogenation into methanol, *ACS Catal.* 10 (2020) 14694–14706.
- [79] Y.J. Zhao, H.H. Zhang, Y.X. Xu, S.N. Wang, Y. Xu, S.P. Wang, X.B. Ma, Interface tuning of Cu^{+/Cu⁰ by zirconia for dimethyl oxalate hydrogenation to ethylene glycol over Cu/SiO₂ catalyst, *J. Energy Chem.* 49 (2020) 248–256.}
- [80] Y. Wang, Y.L. Shen, Y.J. Zhao, J. Lv, S.P. Wang, X.B. Ma, Insight into the balancing effect of active Cu species for hydrogenation of carbon–oxygen bonds, *ACS Catal.* 5 (2015) 6200–6208.
- [81] R.P. Ye, L. Lin, L.C. Wang, D. Ding, Z.F. Zhou, P.B. Pan, Z.H. Xu, J. Liu, H. Adidharma, M. Radosz, M.H. Fan, Y.G. Yao, Perspectives on the active sites and catalyst design for the hydrogenation of dimethyl oxalate, *ACS Catal.* 10 (2020) 4465–4490.
- [82] J. Pang, M. Zheng, C. Wang, X. Yang, H. Liu, X. Liu, J. Sun, Y. Wang, T. Zhang, Hierarchical echinus-like Cu-MFI catalysts for ethanol dehydrogenation, *ACS Catal.* 10 (2020) 13624–13629.
- [83] Y.Q. Tong, J. Zhou, Y.H. He, P.X. Tu, B. Xue, Y.H. Cheng, J. Cen, Y.F. Zheng, J. Ni, X.N. Li, Structure-activity relationship of Cu species in the ethanol upgrading to n-butanol, *ChemistrySelect* 5 (2020) 7714–7719.